



AFRL-RW-EG-TR-2018-011

**Near-Resonant Thermomechanics of
Energetic and Mock Energetic Composite
Materials, Part II**

**Jeffrey F. Rhoads
Steven F. Son
Patricia Davies
Marcial Gonzalez
Marisol Koslowski**

**Allison Range
Jelena Paripovic
Ankit Agarwal
Akshay Dandekar
Lauren Cooper**

**School of Mechanical Engineering
Purdue University
585 Purdue Mall
West Lafayette, IN 47907**

March 2018

Final Report for period 26 October 2016 – 31 December 2017

Contract No. FA8651-16-D-0287

**Distribution A: Approved for public release; distribution unlimited.
Approval Confirmation 96 TW-2018-0074, dated 15 March 2018**

AIR FORCE RESEARCH LABORATORY, MUNITIONS DIRECTORATE

Air Force Materiel Command • United States Air Force • Eglin Air Force Base

This page intentionally left blank

NOTICE AND SIGNATURE PAGE

Using Government drawings, specifications, or other data included in this document for any purpose other than Government procurement does not in any way obligate the U.S. Government. The fact that the Government formulated or supplied the drawings, specifications, or other data does not license the holder or any other person or corporation; or convey any rights or permission to manufacture, use, or sell any patented invention that may relate to them.

Qualified requestors may obtain copies of this report from the Defense Technical Information Center (DTIC) (<http://www.dtic.mil>).

AFRL-RW-EG-TR-2018-011 HAS BEEN REVIEWED AND IS APPROVED FOR PUBLICATION IN ACCORDANCE WITH ASSIGNED DISTRIBUTION STATEMENT.

FOR THE DIRECTOR:

//SIGNED//

//SIGNED//

//SIGNED//

JOHN D. CORLEY, PhD
Ordnance Sciences Core
Technical Competency Lead
Ordnance Division

C. MICHAEL LINDSAY, PhD
Technical Advisor
Energetic Materials Branch

BRETT KIZER
Work Unit Manager
Energetic Materials Branch

This report is published in the interest of scientific and technical information exchange, and its publication does not constitute the Government's approval or disapproval of its ideas or findings.

This page intentionally left blank

REPORT DOCUMENTATION PAGE			<i>Form Approved</i> OMB No. 0704-		
Public reporting burden for this collection of information is estimated to average 1 hour per response, including the time for reviewing instructions, searching existing data sources, gathering and maintaining the data needed, and completing and reviewing this collection of information. Send comments regarding this burden estimate or any other aspect of this collection of information, including suggestions for reducing this burden to Department of Defense, Washington Headquarters Services, Directorate for Information Operations and Reports (0704-0188), 1215 Jefferson Davis Highway, Suite 1204, Arlington, VA 22202-4302. Respondents should be aware that notwithstanding any other provision of law, no person shall be subject to any penalty for failing to comply with a collection of information if it does not display a currently valid OMB control number. PLEASE DO NOT RETURN YOUR FORM TO THE ABOVE ADDRESS.					
1. REPORT DATE (DD-MM-YYYY) 22-03-2018		2. REPORT TYPE Final		3. DATES COVERED (From - To) 26 Oct 2016 – 31 Dec 17	
4. TITLE AND SUBTITLE Near-Resonant Thermomechanics of Energetic and Mock Energetic Composite Materials, Task 0002			5a. CONTRACT NUMBER FA8651-16-D-0297-0002		
			5b. GRANT NUMBER		
			5c. PROGRAM ELEMENT NUMBER 62602F		
6. AUTHOR(S) Rhoads, Jeffrey, F ; Son, Steven, F ; Davies, Patricia ; Gonzalez, Marcial ; Koslowski, Marisol ; Range, Allison ; Paripovic, Jelena ; Agarwal, Ankit ; Dandekar, Akshay ; Cooper, Lauren			5d. PROJECT NUMBER 25029969		
			5e. TASK NUMBER 0002		
			5f. WORK UNIT NUMBER WOXJ		
7. PERFORMING ORGANIZATION NAME(S) AND ADDRESS(ES) School of Mechanical Engineering, Purdue University 585 Purdue Mall West Lafayette, IN 47907			8. PERFORMING ORGANIZATION REPORT NUMBER		
9. SPONSORING / MONITORING AGENCY NAME(S) AND ADDRESS(ES) Air Force Research Laboratory, Munitions Directorate Ordnance Division, Energetic Materials Branch (AFRL/RWME) Eglin AFB FL 32542-5910 Technical Advisor: C. Michael Lindsay, PhD			10. SPONSOR/MONITOR'S ACRONYM(S) AFRL-RW-EG		
			11. SPONSOR/MONITOR'S REPORT NUMBER(S) AFRL-RW-EG-TR-2018-011		
12. DISTRIBUTION / AVAILABILITY STATEMENT Distribution A: Approved for public release; distribution unlimited. Approval Confirmation 96 TW-2018-0074, Dated 15 March 2018					
13. SUPPLEMENTARY NOTES					
14. ABSTRACT The effort described herein seeks to explore the near-resonant thermomechanics of energetic and mock energetic particulate composite materials. The effort specifically focuses on: (i) characterizing the macroscale, elastic and plastic responses of these materials under various mechanical excitations at a range of ambient temperatures; and (ii) developing preliminary computational modeling tools which can be used to predict material response during energetic material formulation and munitions design.					
15. SUBJECT TERMS Materials; Explosives; Mechanical Vibration; Thermomechanics; Damping; Plasticity					
16. SECURITY CLASSIFICATION OF:			17. LIMITATION OF ABSTRACT	18. NUMBER OF PAGES	19a. NAME OF RESPONSIBLE PERSON Brett W. Kizer
a. REPORT	b. ABSTRACT	c. THIS PAGE			19b. TELEPHONE NUMBER (include area code)
UNCLASSIFIED	UNCLASSIFIED	UNCLASSIFIED	SAR	59	

This page intentionally left blank

TABLE OF CONTENTS

Section	Page
1.0 SUMMARY.....	1
2.0 INTRODUCTION	1
3.0 METHODS, ASSUMPTIONS, AND PROCEDURES.....	2
3.1 Sample Preparation	2
3.2 Macroscale Thermomechanical Testing	4
3.3 Dissipative Modeling and Material Property Parameter Estimation	5
3.4 Endochronic Plasticity Modeling.....	8
3.5 Crystal-Binder Interface Modeling.....	13
4.0 RESULTS AND DISCUSSION	15
4.1 Macroscale Thermomechanical Testing Results	15
4.2 Dissipative Modeling and Material Property Parameter Estimation	22
4.3 Endochronic Plasticity Model Results	31
4.4 Crystal-Binder Interface Results.....	41
5.0 CONCLUSIONS.....	42
6.0 REFERENCES	43
APPENDIX.....	45

LIST OF FIGURES

Figure	Page
1	Mold assembly used to produce the 10-pack 1 in diameter, 1 in high cylindrical Samples3
2	Mold assembly for the 7 in x 10 in x 0.5 in rectangular plate samples with intentional stress concentrations. The dimensioned drawing on right (note the dimensions are in inches) shows the location and size of the stress concentrations on the mold insert. The perimeter of the plate sample is represented by the brown dashed line3
3	A schematic of the experimental setup with the (a) FLIR thermal camera, (b) PSV-400 laser Doppler vibrometer, and (c) electrodynamic shaker4
4	The different PBXN-109 formulated (mock) samples with different compositions and geometries that are subjected to sinusoidal and random base excitation testing5
5	(a) The experimental setup showing the MTS Criterion C43, the workstation controlling the machine and the test sample (the one shown is a 1 in × 1 in cylindrical sample composed of 100% HTPB) (b) The stress-strain response of a 100% HTPB sample to cyclic compressive loading12
6	An image of the mesh used in the FEM simulations14
7	Experimental H1 mechanical frequency response estimator of a 85% solids loading – 0% additive content plate at 2.44 g RMS excitation from 10 to 1000 Hz. The solid lines represent data obtained from the geometric center of the sample, and dashed lines represent data obtained from an offset point. Data is presented for (a) the entire excited range and (b) the 40 Hz span surrounding the first resonant frequency.....16
8	Experimental H1 mechanical frequency response estimator of a 85% solids loading – 15% additive content plate at 2.44 g RMS excitation from 10 to 1000 Hz. The solid lines represent data obtained from the geometric center of the sample, and dashed lines represent data obtained from an offset point. Data is presented for (a) the entire excited range and (b) the 50 Hz span surrounding the first resonant frequency.....17
9	Experimental H1 mechanical frequency response estimator of a 85% solids loading – 30% additive content plate at 2.44 g RMS excitation from 10 to 1000 Hz. The solid lines represent data obtained from the geometric center of the sample, and dashed lines represent data obtained from an offset point. Data is presented for (a) the entire excited range and (b) the 50 Hz span surrounding the first resonant frequency.....17
10	A comparison of the experimentally obtained plate surface temperature versus time in response to a 2, 3, 4, and 5 g harmonic excitation near the first resonant frequency for a representative plate of (a,b) 85% solids loading with 0% additive content, (c,d) 85% solids loading with 15% additive content, and (e,f) 85% solids loading with 30% additive content. The colored envelope indicates one standard deviation for each trial. Data are presented for the (a,c,e) mean and (b,d,f) maximum plate surface temperature versus time. The legend indicates the forcing level for each respective test18

11	Experimental H1 mechanical frequency response estimator of an (a) 85% solids loading – 0% additive content plate and an (b) 85% solids loading – 15% additive content plate with intentional stress concentrations at three levels of excitation. The red, green, and blue curves depict responses at 2.44, 1.86, and 1 g RMS, respectively. The solid lines represent data obtained from the geometric center, and the dashed lines represent data obtained from an offset point.	19
12	A comparison of the experimentally obtained plate surface temperature versus time in response to a 2 g harmonic excitation near the first resonant frequency for plates of 85% solids loading with 0% additive content and 85% solids loading with 15% additive content. Data is presented for the (a) mean and (b) maximum plate surface temperature versus time. The legend indicates the plate sample tested for each profile, and the physical location on the top surface of the plate.	20
13	Numerically simulated plate surface temperatures versus time in response to a 2 g excitation near the first resonant frequency for a representative plate of 85% solids loading with 0% additive content. Data are presented for the (a) mean and (b) maximum plate surface temperatures versus time	22
14	The magnitude of the frequency responses estimates generated from random base excitation tests on P85 S100 A00. The excitation power spectral density was set at 0.025 g ² /Hz. The spectral resolution is 0.73 Hz. A Hann window with 50% overlap was used in estimation with 143 segments averaged. Each color represents results from a different day of testing.	22
15	The relative acceleration envelope results obtained from P00 Q000 Q00 C03. The sample was excited at 5 g base excitation from 8 Hz to 68 Hz for 60 s at 1 Hz/s. Each color represents results from a different day of testing. The shading are different tests on the same day from dark to light.	23
16	Results from random base excitation for the PBXN-109 formulated (mock) samples excited for 100 s from 10 Hz to 1000 Hz at 0.025 g ² /Hz. Solid lines denote the estimated magnitude of H and the dashed line denotes its respective coherence. Red denotes results for sample P00 Q000 Q00 C0#, green is for P85 S100 Q00 C0#, and blue is for P85 S070 A30 C0# for (a) large cylinders (3 in tall/diameter) and (b) small cylinders (1 in tall/diameter).....	24
17	The magnitude of the viscoelastic kernel frequency response derived by fitting the nonlinear viscoelastic model to data from the random base excitation test on P85 S070 A30. The blue line is the <i>G</i> response of the viscoelastic term. The black and gray lines are of the different fits for <i>M</i> varying from 10 to 60 in 10 step increments.	25
18	The magnitude of the viscoelastic frequency response estimates of sample P00 Q000 Q00 at various stages in the iterative system identification process. The results of H1 estimation from the time histories generated in the previous step in the algorithm are shown by the red line, and the estimated digital filter's frequency response is the green line. Results are shown for iterations: 1, 20, 60, 120, and 180. The blue line defines which portion of the H1 estimate of the frequency response function (red) was used in the estimation process [$f = \dot{z}$, $M_1 = 40$, $M = 20$].....	27

19	The steps in the iterative parameter estimation approach	28
20	A flow chart of how the 11 functions submitted as part of this report feed into each other to allow the user to investigate the repeatability and experimental set up of the samples.	30
21	(a) Simple compression stress-strain responses of P85 S100 Q00 C00 (green curve, aged 10 days), P85 S100 Q00 C01 (blue curve, aged 19 days) and P85 S100 Q00 C08 (red curve, aged 26 days). (b) Configuration of P85 S100 Q00 C00 specimen at 7% deformation	33
22	Cyclic compressive stress-strain responses of (a) P85 S100 Q00 C05 (peak load 50 N, aged 19 days), (b) P85 S100 Q00 C06 (peak load 75 N, aged 21 days), (c) P85 S100 Q00 C03 (peak load 125 N, aged 19 days), and (d) P85 S100 Q00 C04 (peak load 175 N, aged 19 days), compared with the three simple compression curves from Figure 21a	34
23	(a) Simple compression stress-strain responses of P85 S085 A15 C02 (red curve, aged 1 day), P85 S085 A15 C04 (blue curve, aged 6 days) and P85 S085 A15 C05 (green curve, aged 6 days). (b) Configurations of the three tested specimens at 30% deformation	35
24	Cyclic compressive stress-strain responses of (a) P85 S085 A15 C00 (strain cycling between 10% - 20%, aged 15 days) and (b) P85 S085 A15 C01 (strain cycling between 1% - 2%, aged 9 days), compared with the three simple compression curves from Figure 23a	35
25	Cyclic compressive stress-strain responses of (a) P85 S085 A15 C03 (peak load 175 N, aged 1 day) and (c) P85 S085 A15 C06 (peak load 175 N, aged 6 days), compared with the three simple compression curves from Figure 22a. Subfigures (b) and (d) represent the final configuration of the samples after completing the tests shown by (a) and (c) respectively	36
26	(a) Simple compression stress-strain response of P85 S070 A30 C01 (red curve, aged 6 days). (b) Configuration of the specimen at 30% deformation	37
27	Cyclic compressive stress-strain response of (a) P85 S070 A30 C02 (peak load 75 N, aged 6 days, compared with the simple compression curve of P85 S070 A30 C01 from Figure 26a. Subfigure (b) represents the final configuration of the sample after completing the test.....	37
28	The effective stress at instability vs. aluminum content for the mock energetic specimens	38
29	The stagger algorithm for finite-strain model calibration	39
30	Calibration results for Pure Binder and P85 S085 A15 C00 specimens. The black dots indicate experimental data while red curve indicates calibrated model curve.....	40
31	The simulated temperature on the top surface of the Sylgard block at $t = 10$ s for cases (i) and (ii)	41
32	The simulated temperature on the top surface of the Sylgard block at $t = 10$ s for cases (iii) and (iv)	41

LIST OF TABLES

Table		Page
1	A summary of experimental testing status of the PBXN-109 mock samples, where F denotes Fracture and Day 0 corresponds to the sample cure date. (*) Day 1 for this sample is the first day of testing and not the date cured, the first test was performed about 6 months after curing. The days highlighted in red indicate the tests conducted since September 1 st , 2016	6
2	Thermal properties of HMX	15
3	A comparison of the mean and maximum temperature increase under ambient and insulated thermal boundary conditions for the minimum and maximum additive content samples.....	20
4	A summary of the experiments performed on three different PBXN-109 (mock) specimens (# denotes the number of cycles).....	32
5	Calibrated parameter values for the Pure Binder and P85 S085 A15 C00 specimens.....	40

This page intentionally left blank

1. SUMMARY

The effort described herein seeks to explore the near-resonant thermomechanics of energetic and mock energetic particulate composite materials. The effort specifically focuses on: (i) characterizing the macroscale, elastic and plastic responses of these materials under various mechanical excitations at a range of ambient temperatures; and (ii) developing preliminary computational modeling tools which can be used to predict material response during energetic material formulation and munitions design. Key topics described herein include: sample preparation; macroscale thermomechanical modeling and experimentation; dissipative modeling and system identification; and endochronic plasticity modeling and model validation.

2. INTRODUCTION

The effort described herein seeks to explore the near-resonant thermomechanics of energetic and mock energetic particulate composite materials, building upon both the prior work of the PIs (see, for example, [1-6]) and prior, related work in the field pertaining to the periodic excitation of energetic materials (see, for example, [7-8]) and hot-spot formation (see, for example, [9]). The effort specifically focuses on: (i) characterizing the macroscale, elastic and plastic responses of these materials under various mechanical excitations at a range of ambient temperatures; and (ii) developing preliminary computational modeling tools which can be used to predict material response during energetic material formulation and munitions design. More specifically, Task Order 0002 spans three inter-related research tasks:

- Task 1 – Macroscale Structural and Mechanical Modeling: This task emphasizes further development of macroscale, distributed-parameter and lumped-mass, combined structural and thermal models of mock energetic and energetic materials subjected to mechanical vibration. The models are designed to be amenable to a variety of particle/binder material systems, a range of input excitations (including those leading to large elastic and plastic deformations), and various ambient temperatures. Particular emphasis has been placed on systems with macroscopic geometric discontinuities/stress concentrations (e.g., cracks, steps in geometry, and intentional holes), alternate sample geometries, and less traditional binder systems (e.g., those with a high degree of compliance or the converse). These models are being validated experimentally.
- Task 2 – Modeling of Damping and Dissipation: This task emphasizes the development of refined, macroscale dissipation/damping models for mock energetic and energetic materials subjected to mechanical vibration. Particular emphasis has been placed on less traditional binder systems and on characterizing the ability of the damping models and system identification procedure developed in a prior period of performance to *predict* experimentally-observed phenomena.
- Task 3 – Computational Mechanics Tool Development: This task emphasizes the development of constitutive models for mock energetic and energetic materials that account for nonlinear stress-strain dependencies due to damage, rate-dependent and rate-independent dissipative properties, as well as temperature-dependent properties, and their distillation into computational tools suitable for use in energetic material formulation or munitions design. Particular emphasis has been placed on the continued development of an endochronic material model, preliminary experimental validation of this model, and exploring how this model can be mathematically coupled with the viscoelastic models

being developed as part of Tasks 1 and 2. In addition, preliminary efforts were made to distill lessons learned from crystal-scale computational models into structural-scale models via "effective material properties" or an alternate multi-scale approach.

This final report details the various advancements made by the principal investigators and their research assistants over the noted period of performance. The reader should note that all of the research activities described herein are slated to continue in a *big-picture sense*, and thus the methodologies, results, and perspectives detailed herein represent only a *snapshot of ongoing research*.

The subsequent sections are organized in a traditional sense with methodologies, key results, and discussion provided in turn. Discussions of sample preparation; macroscale thermomechanical modeling and experimentation; dissipative modeling and parameter estimation; and endochronic plasticity modeling are provided in Sections 3 and 4.

3. METHODS, ASSUMPTIONS, AND PROCEDURES

3.1 Sample Preparation

Particulate composite mock energetic materials in a variety of geometries were fabricated with the goal of studying the bulk heating due to mechanical vibration. The samples prepared are variations based upon the PBXN-109 formulation given by Hamshere et al. [10], with sugar replacing the RDX unless otherwise noted. A summary of the formulation variation and fabrication process is presented in the previous annual report [11].

The formulations were cast into various mold geometries. In addition to the cylinder and plate geometries detailed previously, two new molds were designed to produce larger batches of small cylinders, as well as plate samples with intentional stress concentrations. The sample sets of 1 in diameter, 1 in high cylinders were used both in the calibration of the endochronic plasticity model, as well as the uniaxial compression tests (Note: sample dimensions are often provided in standard units, as that is what the corresponding molds were fabricated using). The plate samples with a crack, step, and hole incorporated into the geometry were used in thermomechanical characterization to determine the effect of stress concentrations on the heating of mock energetic materials under periodic loading. The mold assemblies used are shown in Figures 1-2.

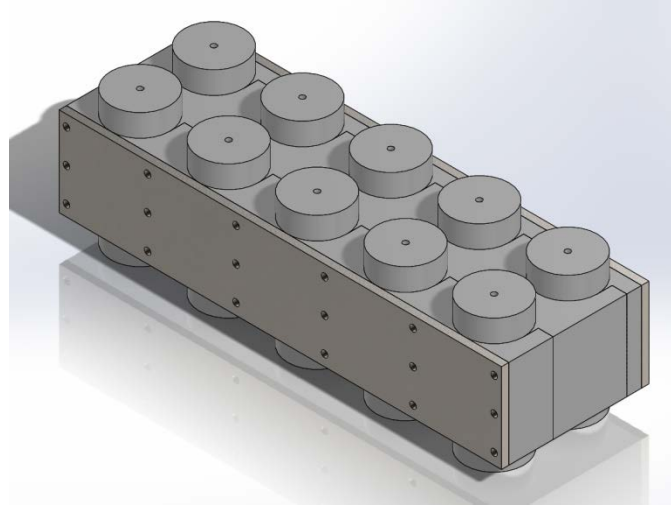


Figure 1. Mold assembly used to produce the 10-pack 1 in diameter, 1 in high cylindrical samples

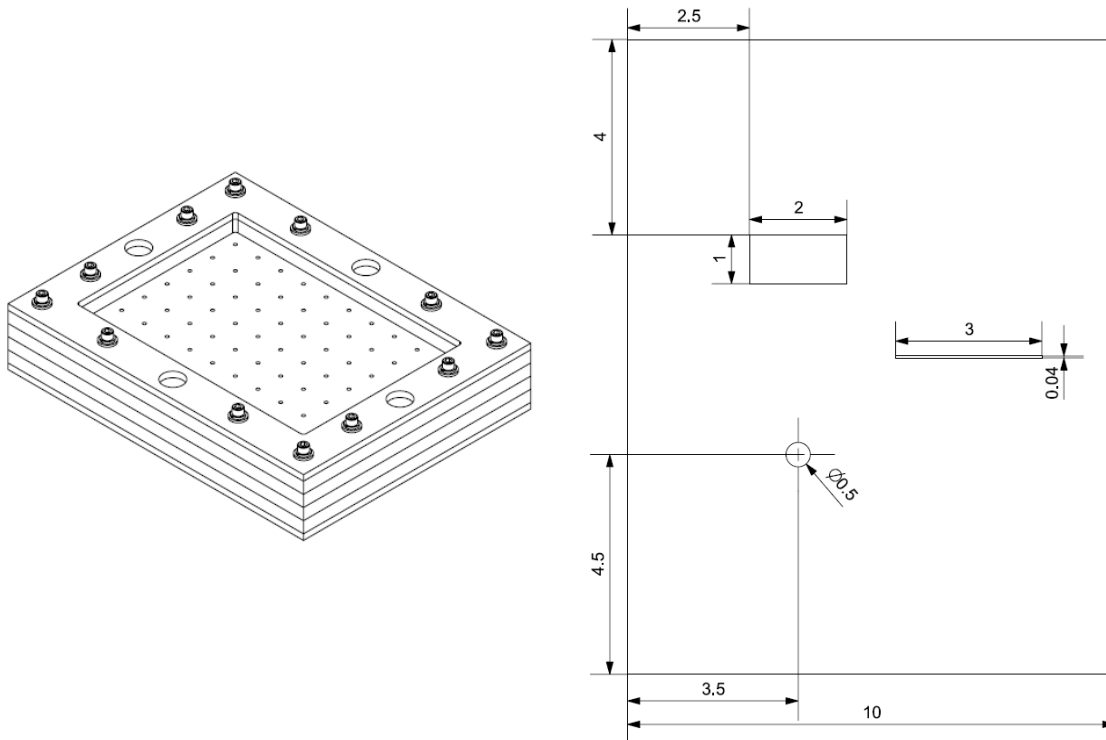


Figure 2. Mold assembly for the 7 in x 10 in x 0.5 in rectangular plate samples with intentional stress concentrations. The dimensioned drawing on right (note the dimensions are in inches) shows the location and size of the stress concentrations on the mold insert. The perimeter of the plate sample is represented by the brown dashed line.

3.2 Macroscale Thermomechanical Testing

Over the past year, significant effort has been made to increase the understanding of particulate composite mock energetic plates excited by mechanical vibration. As part of this effort, experiments were conducted on newly-fabricated plate samples in order to investigate the effect of increased excitation amplitude and intentional stress concentrations on the thermal and mechanical response of representative samples. The plate samples tested consisted of hydroxyl-terminated polybutadiene binder (HTPB) with varying ratios of spherical aluminum powder (with an approximate diameter of 25 μm) and sucrose crystals (sieved to be in the 106-355 μm diameter range), chosen as a rough mechanical mock to RDX. These samples were tested both with and without intentional stress concentrations.

Experiments were conducted using three major pieces of equipment. The plate samples were mounted in a pre-existing fixture to approximate a clamped-free-clamped-free (CFCF) boundary configuration and placed upon a TIRA 59335/LS AIT-440 electrodynamic shaker. A Polytec PSV-400 scanning laser Doppler vibrometer was then employed to record frequency responses and operational deflection shapes. Simultaneously, a FLIR A325 infrared camera was used to capture the temperature distribution of the top surface of the plate using infrared thermography. The experimental setup is depicted in Figure 3.

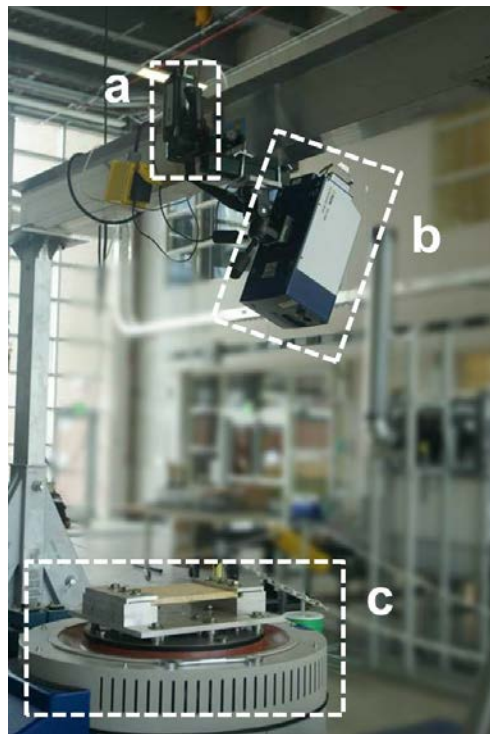


Figure 3. A schematic of the experimental setup with the (a) FLIR thermal camera, (b) PSV-400 laser Doppler vibrometer, and (c) electrodynamic shaker

3.3 Dissipative Modeling and Material Property Parameter Estimation

The goal of this task was to observe and characterize the mechanical material behavior of the mock energetic materials. This was achieved by conducting low frequency random and swept sine base excitation tests on mass-material systems, and then using a parameter estimation methodology to extract those material parameters that characterize the stiffness, damping and viscoelastic properties of the materials.

3.3.1 Experimental Work

In this performance period we continued to conduct swept sine and random base excitation testing on the PBXN-109 formulated (mock) samples, which are shown in Figure 4. A summary of the tests that have been completed in the period are shown in Table 1.

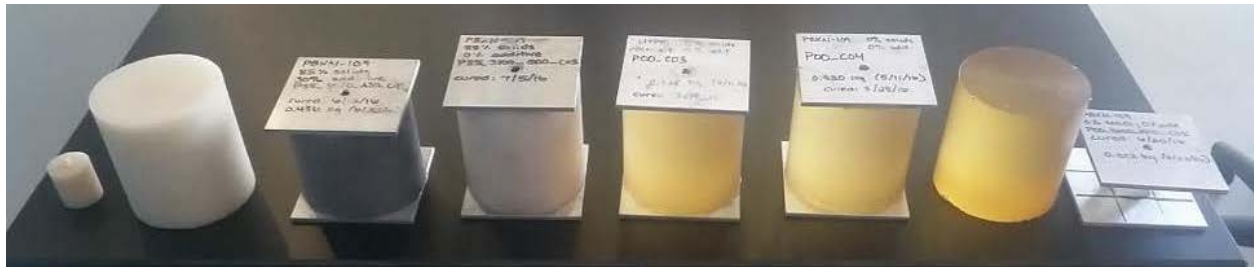


Figure 4. The different PBXN-109 formulated (mock) samples with different compositions and geometries that are subjected to sinusoidal and random base excitation testing

For the swept sine tests, on each day of testing, three 60 s sinusoidal sweeps were conducted at a sweep rate of 1 Hz/s, with the start of each of the sweep staggered 30 min apart. The frequency range was selected such that the first resonance frequency of the mass-material system was captured during the sweep. The base excitation level was varied from 5 g to 1 g to minimize sample fracturing. For the random base excitation tests, on each day of testing, three random base excitation tests were conducted, again with the tests conducted 30 min apart. Each random base excitation test lasted for 100 s. The power spectral density of the base excitation was flat from 10 Hz to 1000 Hz at a $0.025 \text{ g}^2/\text{Hz}$ excitation level. The signals were passed through a Wavetek 852 low pass filter set at 1,500 Hz prior to being acquired at 6,000 samples/s using a National Instruments 24-bit data acquisition system. The geometry, composition, and cure date of the samples being tested, along with the testing status, are given in Table 1. The days highlighted in red denote tests that have been conducted after September 1st, 2016. Note that each day listed in the table represents three consecutive tests conducted 30 min apart.

Table 1. A summary of experimental testing status of the PBXN-109 mock samples, where *F* denotes Fracture and Day 0 corresponds to the sample cure date. (*) Day 1 for this sample is the first day of testing and not the date cured, the first test was performed about 6 months after curing. The days highlighted in red indicate the tests conducted since September 1st, 2016.

Sample ID	Random Base Excitation		Harmonic Base Excitation	
	Forcing Level	Day #	Forcing Level	Day #
P00 Q000 Q00 C01 (HTPB 100% Solids 0%) Diam: 1" Height: 1" Cure Date: 2/29/2016	0.050 g ² /Hz	77,86 ^F	2 g	77
			4 g	77
P00 Q000 Q00 C02 (HTPB 100% Solids 0%) Diam: 1" Height: 1" Cure Date: 2/29/2016	0.025 g ² /Hz	86, 102	1 g	109
	0.050 g ² /Hz	86, 102	2 g	109^F
P00 Q000 Q00 C03 (HTPB 100% Solids 0%) Diam: 3" Height: 3" Cure Date: 3/15/2016	0.025 g ² /Hz	84, 123	2 g	62,85,92,99
	0.050 g ² /Hz	62,84, 123	3 g	92
			5 g	62,85,99
P00 Q000 Q00 C04 (HTPB 100% Solids 0%) Diam: 3" Height: 3" Cure Date: 3/28/2016	0.015 g ² /Hz	78	2 g	79,86
	0.025 g ² /Hz	64,78	3 g	79,86
	0.050 g ² /Hz	78	5 g	64,79
P00 Q000 Q00 C05 (HTPB 100% Solids 0%) Diam: 1" Height: 1" Cure Date: 6/20/2016	0.025 g ² /Hz	4,25		
	0.050 g ² /Hz	4,25 ^F		
P85 S070 A30 C02 (HTPB 15% Solids 85%) Diam: 1" Height: 1" Cure Date: 8/9/2016	0.010 g ² /Hz	55		
	0.005 g ² /Hz	227		
P85 S070 A30 C03 (HTPB 15% Solids 85%) Diam: 3" Height: 3" Cure Date: 6/13/2016	0.025 g ² /Hz	15,29,36, 218,225		
	0.050 g ² /Hz	15,29,36		
P85 S085 A15 C02 (HTPB 15% Solids 85%) Diam: 1" Height: 1" Cure Date: 6/13/2016	0.005 g ² /Hz	207,247		
P85 S100 Q00 C03 (HTPB 15% Solids 85%) Diam: 3" Height: 3" Cure Date: 9/19/2016	0.025 g ² /Hz	15, 211,218,228		
	0.050 g ² /Hz	15, 255		
P85 S100 Q00 C01 (HTPB 15% Solids 85%) Diam: 1" Height: 1" Cure Date: 9/28/2016	0.025 g ² /Hz	69^F		
H00 Q000 Q00 C03* (HTPB 100% Solids 0%) Diam: 3" Height: 2.4" Cure Date: 2012	0.025 g ² /Hz	1681	5 g	1,2,19,24,71,109,138, 1681
L85 S100 Q00 C01 (HTPB 15% Solids 85%) Diam: 3" Height: 3" Cure Date: 4/13/2017	0.025 g ² /Hz	71		

The frequency response functions and the coherence functions relating the base acceleration and the acceleration of the top plate relative to the base were estimated from the measurements taken in the random tests (see [11] for additional details). The power spectral density and cross spectral density estimates were calculated by using the Matlab *pwelch* and *cpsd* built in functions. The segment size was chosen to give a frequency resolution of 0.73 Hz and each data segment was windowed with a Hann window. The frequency response function (H) and the coherence function were estimated. For the sweep tests, the envelope of the relative response during the sweep was plotted against the frequency of the base excitation signal. When significant nonlinearity was present, the response at the excitation frequency was first extracted by using modulation and filtering, and the envelope of the resulting signal was plotted.

3.3.2 Modeling Work

In this performance period we have continued to improve the iterative parameter estimation approach that was previously outlined in [11]. Recall that the ten step process uses a continuous time system identification approach to estimate the stiffness and damping parameters and a Prony analysis approach to estimate the viscoelastic parameters. This past year we have worked on improving the model order selection process, the stability of the estimated viscoelastic filter, and the convergence criteria. Lastly, in this report we present a formal derivation of the model about the settling point, and for the generic viscoelastic term, so that we can relate system parameters (stiffness, damping and viscoelastic terms relating relative velocity rate viscoelastic forces) to material parameters (e.g., Young's Modulus and viscoelastic terms relating strain rate to pressure).

Model Derivation Summary

A detailed derivation of the model about the settling point was presented in the April 2017 monthly project report, the main conclusions are presented here. Consider the generic equation of motion of a base excitation mass-material system containing a damping term (\bar{c}), polynomial stiffness (\bar{k}), and viscoelastic term (\bar{v}), it is of the form:

$$m\ddot{z} + \bar{c}(\dot{z}, z + z_0) + \sum_{i=1}^N \bar{k}_i (z + z_0)^i + \bar{v}((z + z_0), \dot{z}) = -m\ddot{y} - mg \quad (1)$$

where m is the mass, z is the relative motion about the settling point, and z_0 is the settling displacement. Defining

$$c(\dot{z}, z) = \bar{c}(\dot{z}, z + z_0) - \bar{c}_0 \quad (2)$$

$$v(\dot{z}, z) = \bar{v}((z + z_0), \dot{z}) - \bar{v}_0 \quad (3)$$

and

$$\bar{c}_0 + \sum_{i=1}^N \bar{k}_i (z_0)^i + \bar{v}_0 = -mg \quad (4)$$

we can simplify and subtract like terms to yield the simplified equation of motion about the settling point; it is of the form:

$$m\ddot{z} + c(\dot{z}, z) + \sum_{i=1}^N k_i z^i + v(z, \dot{z}) = -m\ddot{y} \quad (5)$$

Furthermore, the polynomial stiffness terms about the settling point can be defined as:

$$k_p = \sum_{n=p}^N z_0^{(n-p)} \bar{k}_n \frac{n!}{p!(n-p)!} \quad (6)$$

where N is the polynomial order, and n are integers from 1 to N . For different nonlinear expressions of damping, stiffness, and the viscoelastic term, the expansion about the settling point may yield slightly different expressions of the final equation and these need to be derived on a case by case basis.

Our current parameter estimation process uses the system model about the operating point (Equation 5) to estimate the system parameters (k_1, k_2, c , etc.). These estimated parameters may be related to its respective system material model (Equation 1) terms ($\bar{k}_1, \bar{k}_2, \bar{c}$, etc.). Using the geometric properties, the system material model terms ($\bar{k}_1, \bar{k}_2, \bar{c}$, etc.) can be related to the Young's Modulus and one can write the basic constitutive material model in terms of stress and strain.

3.4 Endochronic Plasticity Modeling

Energetic composite materials have been found to exhibit a significant nonlinear elasto-plastic stress-strain response in the range of finite deformations under cyclic load, without a distinctive yield surface. Consequently, assumptions of small deformations and linear-elastic material, and plasticity modeling using classical plasticity theories that require a yield surface, may prove to be insufficient in predicting their mechanical response, necessitating the use of a finite-strain formulation that accounts for nonlinear elasticity and yield surface-free plasticity.

This report summarizes our research efforts in the direction of modeling the cyclic loading behavior of energetic composite materials, with the goal of building a computational tool capable of predicting such behavior. A finite strain formulation that used Ogden's model [12,13] with a material incompressibility assumption to predict the elastic response, and a yield-surface free endochronic plasticity model proposed by Valanis [14] to account for irreversible deformations, was developed. A computationally efficient central difference method-based numerical algorithm proposed by Suchocki [15] was adapted to perform the necessary calculations at each load step. Calibration of the model parameters was performed using experimental data obtained from compressive cyclic tests of mock energetic material specimens.

3.4.1 A Finite Strain Formulation for Mock Energetic Materials

For an initially virgin, isotropic material subjected to a general loading configuration, the Second Piola-Kirchhoff stress tensor is given by:

$$\mathbf{S} = \mathbf{S}^e + \mathbf{S}^i \quad (7)$$

where \mathbf{S}^e and \mathbf{S}^i are respectively the elastic and inelastic contributions to the total stress. The following sections elaborate on the formulation proposed to obtain the respective contributions.

Elasticity Model Formulation

Very recently, efforts in the direction of elasticity modeling of energetic composite materials have been made by Davies and Paripovic [6,16-18], who proposed the following equation to model the elastic stress-strain response of energetic materials under uniaxial compressive loading

$$\sigma_3^e = \frac{1}{\epsilon_3 + 1} \sum_{k=1}^M \frac{2\mu_k}{\alpha_k^2} [(\epsilon_3 + 1)^{\alpha_k} - 1] \quad (8)$$

for compressive loading in the 3-direction, σ_3^e is the stress, ϵ_3 is the strain, and μ_k and α_k are $2M$ empirically determined material parameters. The ground state shear modulus μ can be related to the parameters μ_k by

$$\mu = \sum_{k=1}^M \mu_k \quad (9)$$

Equation 8 has proven to be very useful and efficient in predicting the uniaxial compressive elastic response of energetic materials, thanks to its simplicity and sufficient flexibility. However, it cannot be used for predicting material behavior in response to a general loading configuration. To alleviate this limitation, the stress-strain response can be described by a three-dimensional Ogden strain energy function ψ , given by

$$\begin{aligned} \psi &= \psi_{\text{iso}}(\bar{\lambda}_1, \bar{\lambda}_2, \bar{\lambda}_3) + \psi_{\text{vol}}(J) \\ &= \sum_{k=1}^M \frac{2\mu_k}{\alpha_k^2} (\bar{\lambda}_1^{\alpha_k} + \bar{\lambda}_2^{\alpha_k} + \bar{\lambda}_3^{\alpha_k} - 3) + \psi^{\text{vol}}(J) \end{aligned} \quad (10)$$

In the above equation, the strain energy function has been decoupled into isochoric (ψ_{iso}) and volumetric (ψ_{vol}) contributions. $\bar{\lambda}_1$, $\bar{\lambda}_2$ and $\bar{\lambda}_3$ are the isochoric material stretches in three respective coordinate directions, and (μ_k, α_k) are the material parameters discussed before. The volumetric part ψ_{vol} can be defined according to Netzker [9] by

$$\psi_{\text{vol}} = \kappa(J - \ln J - 1) \quad (11)$$

where J represents the change in volume, given by $J = \lambda_1 \lambda_2 \lambda_3$, and κ is the bulk modulus. The elastic Cauchy stress tensor \mathbf{S}^e can be obtained from the strain energy function ψ in Equation 10 by using the relation

$$\begin{aligned} \mathbf{S}^e &= \mathbf{S}_{\text{iso}}^e + \mathbf{S}_{\text{vol}}^e \\ &= J^{-2/3} \sum_{p=1}^3 \frac{1}{\bar{\lambda}_p} \left[\frac{\partial \psi_{\text{iso}}}{\partial \bar{\lambda}_p} - \frac{1}{3} \left(\frac{\partial \psi_{\text{iso}}}{\partial \bar{\lambda}_1} + \frac{\partial \psi_{\text{iso}}}{\partial \bar{\lambda}_2} + \frac{\partial \psi_{\text{iso}}}{\partial \bar{\lambda}_3} \right) \right] \mathbf{n}_p \otimes \mathbf{n}_p + J \frac{\partial \psi_{\text{vol}}}{\partial J} \mathbf{C}^{-1} \end{aligned} \quad (12)$$

where \mathbf{n}_p ($p = 1, 2, \text{ and } 3$) are unit vectors in the principal directions, and \mathbf{C} is the right Cauchy-Green deformation tensor given by

$$\mathbf{C} = \sum_{p=1}^3 \lambda_p^2 \mathbf{n}_p \otimes \mathbf{n}_p \quad (13)$$

Plasticity Model Formulation

Apart from elastic behavior, energetic materials have been found to exhibit significant plastic (irreversible) deformations, especially during cyclic loading. As already discussed, these materials may exhibit significant nonlinear stress-strain behavior in both the elastic and inelastic range, without a distinctive yield point. Classical plasticity theories require a yield surface for predicting material behavior, and hence may not be applicable to model these materials.

The endochronic plasticity theory developed by Valanis [14] is a hereditary plasticity theory that assumes that the state of stress about an elasto-plastic material point is dependent on the strain or deformation history of that point. The strain history is represented by a variable called the intrinsic time, and the stress evolution is given by the convolution integral between the stress tensor and the memory kernel, which is a scalar function of intrinsic time. Since the theory does not distinguish between the elastic and plastic state of the material, and assumes elasto-plastic behavior at any given load step, a yield surface is not required.

According to Suchocki [15], the endochronic constitutive equation for plastic stress $\mathbf{S}^i = \sum_{j=1}^N \mathbf{S}_j^i$ in the range of finite deformations is given by

$$\mathbf{S}_j^i(t) = \int_0^{z(t)} C_j e^{-\frac{z-\zeta}{\gamma_j}} \frac{\partial \mathbf{S}_{\text{iso}}^e}{\partial \zeta} d\zeta \quad (14)$$

where C_j and γ_j are the kernel parameters, $\mathbf{S}_{\text{iso}}^e$ is the isochoric part of elastic stress, and z and ζ are the intrinsic time scale and intrinsic time measure respectively. The relationship between z and ζ is given by

$$\frac{d\zeta}{dz} = f(z) \quad (15)$$

where $f(z)$ is function that describes the material's hardening or softening behavior as it deforms. Various forms of $f(z)$ have been reported in literature [13,19,20]. However, the one reported by Lin et al. [21] is the most flexible and best suited for cyclic loading. The function is given by

$$f(z) = D(z_{\text{ref}}) - [D(z_{\text{ref}}) - 1]e^{-\beta_1(z-z_{\text{ref}})} \quad (16)$$

where

$$D(z_{\text{ref}}) = \frac{c}{s - (s - 1)e^{-\beta_2 z_{\text{ref}}}} \quad (17)$$

In Equations 16 and 17, c , s , β_1 and β_2 are positive material constants, where $c > s > 1$ signifies hardening and $c < s < 1$ signifies softening behavior [21]. Quantity z_{ref} is the reference intrinsic time scale, that corresponds to the value of z at which the last load reversal occurred. Lin et al. [21] have utilized this function to accurately model the mechanical response of OFHC copper and SAE 4340 steel. However, for modeling energetic composite materials, whose cyclic loading behavior has been found to be highly nonlinear, a more flexible and general form of $f(z)$ may be required. We thus propose a modified form of $f(z)$ given by

$$f(z) = \sum_{m=1}^K D_m(z_{\text{ref}}) - [D_m(z_{\text{ref}}) - 1]e^{-\beta_{1,m}(z-z_{\text{ref}})} \quad (18)$$

where

$$D_m(z_{\text{ref}}) = \frac{c_m}{s_m - (s_m - 1)e^{-\beta_{2,m}z_{\text{ref}}}} \quad (19)$$

The proposed function is an extended form of the material function proposed by Lin et al. [21], modified to be defined as the sum of a series of terms. The proposed function contains $4K$ unknown parameters as opposed to 4 unknown parameters in Lin's function [21]. On account of being more general, the proposed function is believed to serve as a better representative of the hardening/softening behavior of mock energetic materials.

Numerical Procedure for Plastic Stress Calculation

Discretization using the central difference method has been proposed by Suchocki [15] to calculate the inelastic stress at every load step. Using central differences in Equation 14 at load step $(n+1)/2$, one may obtain the inelastic stress at load step $(n+1)$ equal to

$$\mathbf{s}_{n+1}^i = \sum_{j=1}^N \mathbf{s}_{j,n+1}^i = \sum_{j=1}^N \frac{\left(1 - \frac{1}{2\gamma_j} \Delta z_{n+1}\right) \mathbf{s}_{j,n}^i + C_j (\mathbf{s}_{\text{iso},n+1}^e - \mathbf{s}_{\text{iso},n}^e)}{\left(1 + \frac{1}{2\gamma_j} \Delta z_{n+1}\right)} \quad (20)$$

where $\Delta(\cdot)_{n+1} = (\cdot)_{n+1} - (\cdot)_n$. The quantity Δz_{n+1} in Equation 20 can be obtained by using central differences at load step $(n+1)/2$ in the relationship between ζ and z (Equation 15). The discretized relationship is given by

$$\frac{d\zeta}{dz} \cong \frac{\Delta\zeta_{n+1}}{\Delta z_{n+1}} = \sum_{m=1}^K D_m - (D_m - 1)e^{-\beta_{1,m}(z_n + \frac{\Delta z_{n+1}}{2} - z_{\text{ref}})} \quad (21)$$

In Equation 21 above, $\Delta\zeta_{n+1}$ is given by

$$\Delta\zeta_{n+1} = (\Delta\bar{C}_{n+1} : \Delta\bar{C}_{n+1})^{1/2} \quad (22)$$

where \bar{C} is the isochoric part of right Cauchy-Green deformation tensor given by Equation 13.

Substituting Equation 22 into Equation 21 and rearranging, we get

$$\left[\sum_{m=1}^K D_m - (D_m - 1)e^{-\beta_{1,m}(z_n + \frac{\Delta z_{n+1}}{2} - z_{\text{ref}})} \right] \Delta z_{n+1} - (\Delta\bar{C}_{n+1} : \Delta\bar{C}_{n+1})^{1/2} = g(\Delta z_{n+1}) \quad (23)$$

$$= 0$$

Equation 23 above is a function of Δz_{n+1} only, and can be numerically solved using Newton-Raphson method.

3.4.2 Experimental Setup

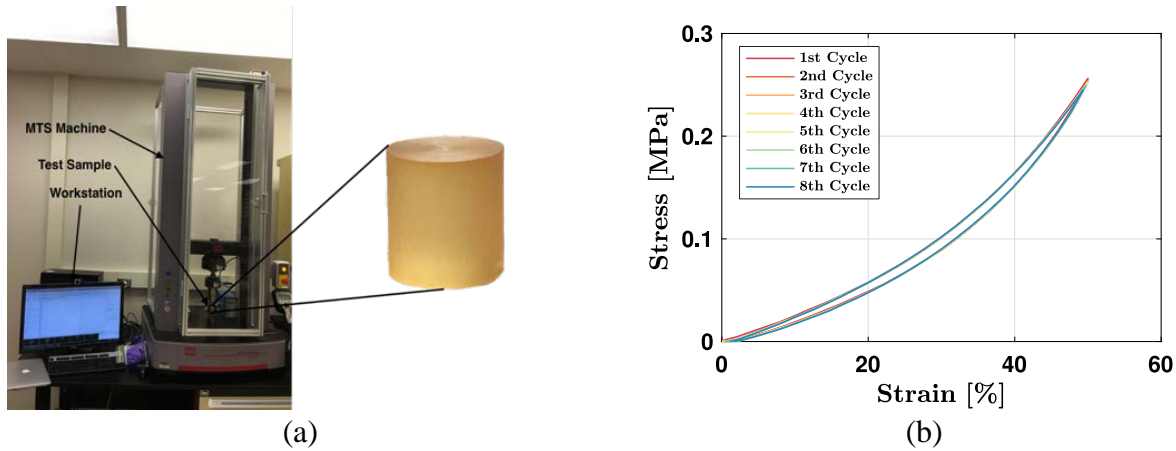


Figure 5. (a) The experimental setup showing the MTS Criterion C43, the workstation controlling the machine and the test sample (the one shown is a 1 in \times 1 in cylindrical sample composed of 100% HTPB) (b) The stress-strain response of a 100% HTPB sample to cyclic compressive loading.

Figure 5a depicts the experimental setup utilized for data collection. The instrument is an MTS Criterion C43 universal testing machine available in the Particle Design and Formulation Lab at Purdue University. The machine can perform cyclic testing at rates up to 100 mm/min, with rated

force capacity up to 50 kN and data acquisition rate up to 1000 Hz, making it suitable for our purposes. It is controlled through a manufacturer-provided, user-friendly software TW Elite.

3.5 Crystal-Binder Interface Modeling

When discrete energetic particles, embedded in a polymer binder, are subjected to high-frequency periodic mechanical excitation, local temperature gains have been observed.

Recent experiments by our team at Purdue University have identified several mechanisms that may affect heat generation. Principally these experiments have indicated that the temperature rise strongly depends upon:

- 1) The geometry and arrangement of the particles in the sample;
- 2) The initial interface damage at the particle/binder interface; and
- 3) The initial microcracks and defects in the particles.

Other hot-spot mechanisms considered in the literature include: the adiabatic compression of trapped gas spaces, void collapse, plastic deformation, heating at crack tips, heating at dislocation pile-ups, friction at crack surfaces, dissipation due to crack propagation, particle/polymer debonding, and viscous heating.

Prior work has demonstrated that the adiabatic compression of gas spaces is a dominant mechanism for liquid explosives [22], but for solid explosives, shock waves are necessary to create sufficient adiabatic heating to increase the temperature sufficiently to initiate [23]. Similarly, to collapse a void in solid explosive requires forces that can likely be provided only by shock waves. Thus, these two mechanisms are not applicable for the regime of velocity and loading considered in this project and can be neglected.

Unfortunately, it is not possible to independently investigate each of the aforementioned physical mechanisms experimentally. Therefore, models have been developed and 3D finite element simulations have been performed to elucidate their relative importance.

3.5.1 The Effect of Particle Distribution

Finite elements simulation of samples with different geometries were performed to investigate the local stresses and the effect of the heat source location on sample temperature. The simulation domain was selected with the same dimensions as the experimental specimen described in [24] and it is shown in Figure 6. It consisted of a Sylgard block of length 8.9 mm, width 6.6 mm, and height 4.5 mm. The three HMX particles had an approximate diameter of 0.8 mm and were placed at the center of the horizontal cross-section such that their distance to the top surface was 1 mm.

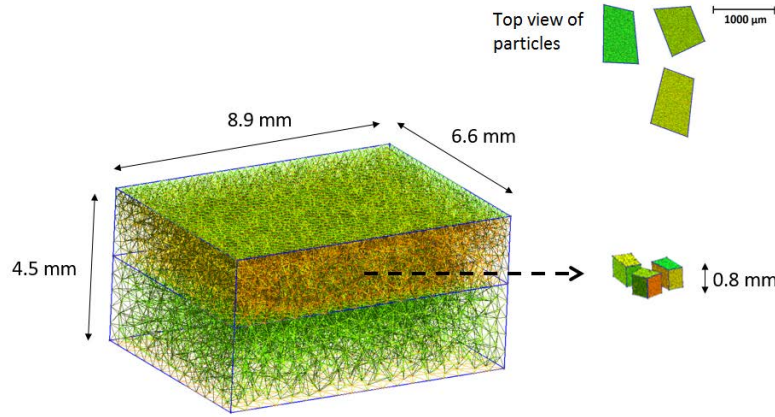


Figure 6. An image of the mesh used in the FEM simulations

3D finite elements simulations were performed to predict the stress and strain fields in the specimen during mechanical excitation. Stress concentrations located at the corners of the particles are observed. These stress concentrations are expected to lead to damage and heat generation. From the finite element simulations, it was clear that the damage will occur initially on the bottom and later on the top surfaces of the particles. To qualitatively understand the effect of the heat source location on the temperature distribution, the heat equation was solved in a 3D finite element mesh. Four cases with different heat source locations were studied: (i) when the source was located at the bottom of one of the particles, (ii) when the source was located at the top of one the particles, (iii) when the sources were located at the bottom of all particles, and (iv) when the sources were located at the top of all particles. The heat source(s) in all of the cases were included such that they cover the entire cross-section of the corresponding particle with a height of $40 \mu\text{m}$. An approximate value of $q_v = 10^9 \text{ W/m}^3\text{s}$ was used.

3.5.2 The Effect of Initial Damage

Due to the high computational cost of solving a dynamic problem with frequencies in the range of 150 kHz to 210 kHz this portion of the current effort focused on the development of a coarse grain model to estimate the evolution of the temperature due to friction at the particle/polymer interface and pre-existing micorcracks in the particles. The temperature changes reported here are just an approximation to decide which mechanisms may be the most important when we run future simulations.

The heating due to interfacial friction at a crack can be estimated from a 1D solution of heat flow equation [25]

$$\Delta T = 2\dot{q} \sqrt{\frac{t}{\pi k \rho c}} \quad (24)$$

where $\dot{q} = \mu \llbracket v \rrbracket \cdot \tau$ is the surface heating due to friction. Here, μ denotes the coefficient of friction, τ denotes the traction at the crack surface and $\llbracket v \rrbracket$ is the velocity jump in the crack or the sliding

velocity between the two crack surfaces. The other material parameters are listed in Table 2.

The finite element simulations suggest that the stresses are of the order of 30 MPa for an excitation frequency of 210 kHz and amplitude of 2 μm . The sliding velocity can be approximated by multiplying the amplitude by the frequency of the applied mechanical excitation as $v \sim 2.645 \text{ m/s}$. Thus, the increase in temperature due to friction at a preexisting crack surface can be calculated to be, $\Delta T \sim 62 \text{ K}$ after 1 μs . The estimation of temperature rise due to debonding and the resulting friction at the interface can be calculated using the same equation given above for friction and gives similar results. The viscous dissipation can be roughly estimated by assuming the entire energy input is utilized in viscous dissipation. This calculation gives a temperature rise of less than 1 μK in 1 μs .

Table 2. Thermal properties of HMX

Property	Value
ρ_0 [kg/m^3]	1903
c [J/kg K]	1576
k [J/m s K]	0.31

3.5.3 Summary

The outcome of the finite element simulations and the coarse grain model help to explore the relative importance of the heating mechanisms at different length and time scales. The most important heating mechanism appears to be friction at preexisting cracks and surface defects between the particle and the polymeric binder. Therefore, it is of key importance to incorporate initial defects as well as particle distribution in various models to assess the risk of initiation.

4. RESULTS AND DISCUSSION

4.1 Macroscale Thermomechanical Testing Results

4.1.1 The Effect of Increased Forcing Levels

All of the transient thermal response results presented at this juncture have been in response to a 2 g sinusoidal excitation at resonance; however, it has been hypothesized that the heat generation would increase significantly as this forcing level was increased. To this end, a set of increased amplitude experiments were performed on a representative plate sample of each 85% solids loading formulation (0%, 15%, and 30% additive content). Each experiment was performed at a sample age of 216 days.

The transient temperature profile over a 60 min window in response to a sinusoidal excitation of 2, 3, 4, and 5 g under convective boundary conditions was recorded using a FLIR thermal camera. Preceding each test, the laser Doppler vibrometer was used to record the mechanical response of the plate under random excitation to monitor resonant frequency shifts and potential structural damage to the sample. The H1 frequency response estimators for a representative plate sample in

response to broadband white noise at a forcing level of 2.44 g RMS are presented in Figures 7-9 for the plates with 85% solids loading and 0%, 15%, and 30% additive content. The legend indicates the forcing level used in the thermal response test following the recording of the respective frequency response.

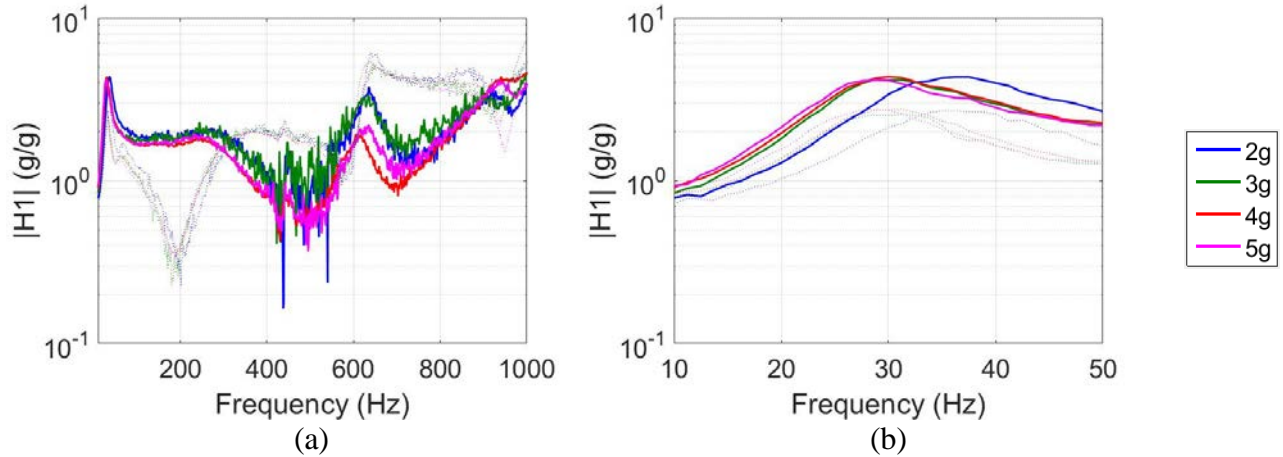


Figure 7. Experimental H1 mechanical frequency response estimator of a 85% solids loading – 0% additive content plate at 2.44 g RMS excitation from 10 to 1000 Hz. The solid lines represent data obtained from the geometric center of the sample, and dashed lines represent data obtained from an offset point. Data is presented for (a) the entire excited range and (b) the 40 Hz span surrounding the first resonant frequency.

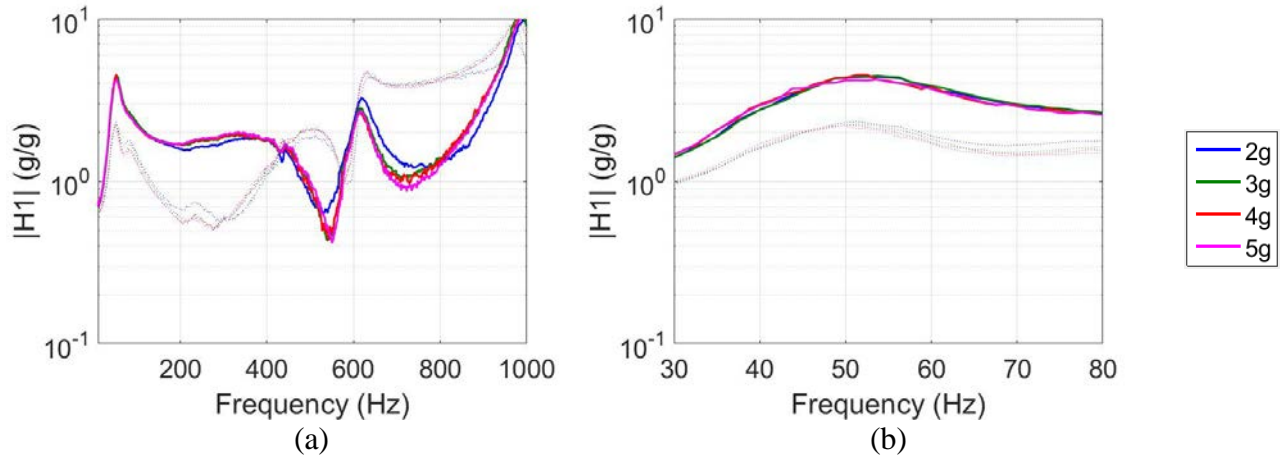


Figure 8. Experimental H1 mechanical frequency response estimator of a 85% solids loading – 15% additive content plate at 2.44 g RMS excitation from 10 to 1000 Hz. The solid lines represent data obtained from the geometric center of the sample, and dashed lines represent data obtained from an offset point. Data is presented for (a) the entire excited range and (b) the 50 Hz span surrounding the first resonant frequency.

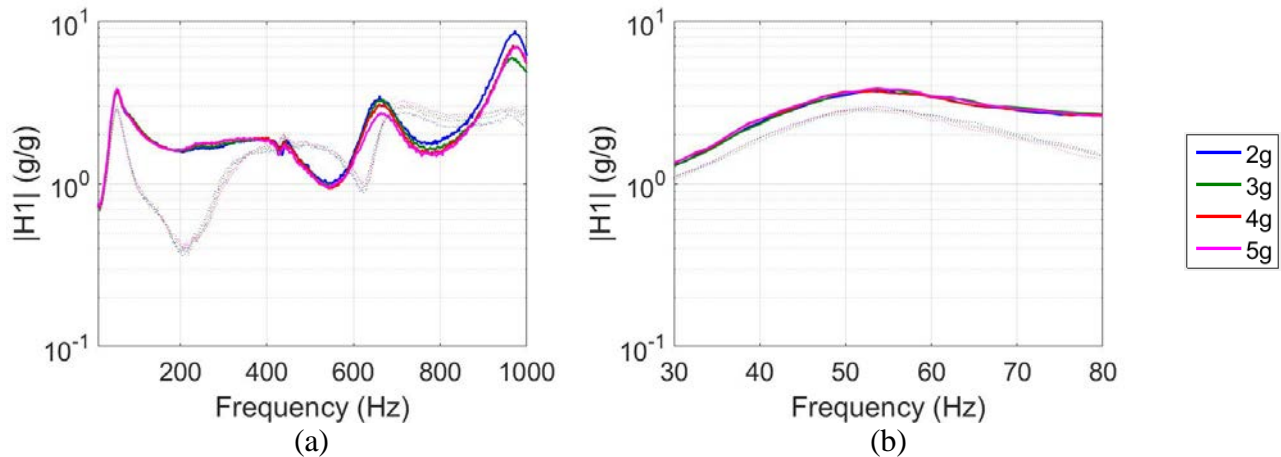


Figure 9. Experimental H1 mechanical frequency response estimator of a 85% solids loading – 30% additive content plate at 2.44 g RMS excitation from 10 to 1000 Hz. The solid lines represent data obtained from the geometric center of the sample, and dashed lines represent data obtained from an offset point. Data is presented for (a) the entire excited range and (b) the 50 Hz span surrounding the first resonant frequency.

The spatial average and maximum surface temperature for a representative plate sample of each of the three formulations over the 60 min window at the first resonant frequency under convective boundary conditions at 2, 3, 4, and 5 g forcing levels are presented in Figure 10, respectively. Note that the temperature rise observed in each subsequent test does increase with forcing level; however, the rise is quite gradual. Interestingly, a significant change was not observed in temperature rise between the 15% and 30% additive content samples.

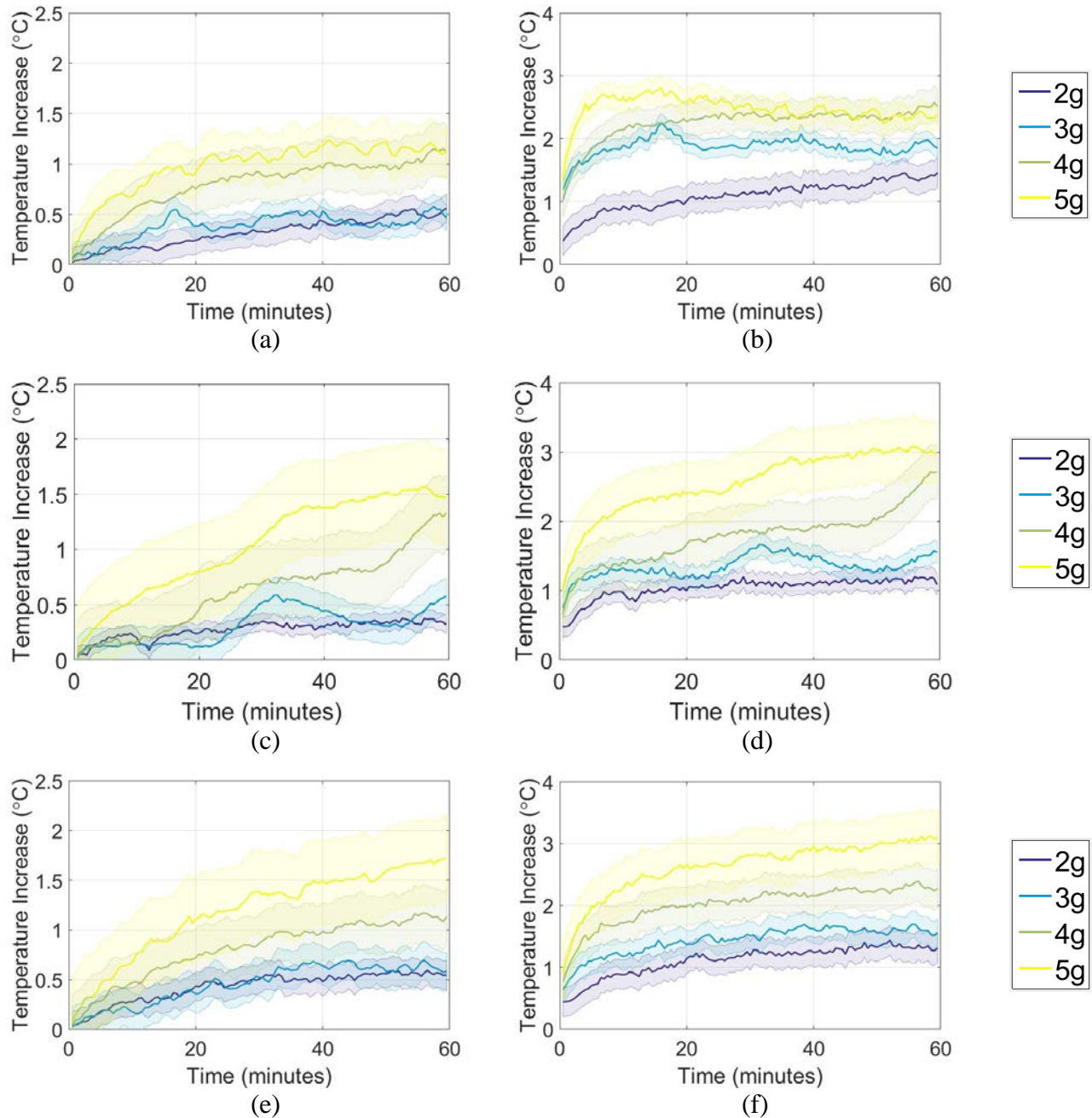


Figure 10. A comparison of the experimentally obtained plate surface temperature versus time in response to a 2, 3, 4, and 5 g harmonic excitation near the first resonant frequency for a representative plate of (a,b) 85% solids loading with 0% additive content, (c,d) 85% solids loading with 15% additive content, and (e,f) 85% solids loading with 30% additive content. The colored envelope indicates one standard deviation for each trial. Data are presented for the (a,c,e) mean and (b,d,f) maximum plate surface temperature versus time. The legend indicates the forcing level for each respective test.

4.1.2 The Effect of Macroscale Intentional Stress Concentrations

The results of an initial investigation of the thermal and mechanical behavior of mock energetic plates with intentional stress concentrations under contact excitation are presented below. The transient temperature profile over a 60 min window in response to sinusoidal excitation of 2 g under convective boundary conditions was recorded using a FLIR thermal camera. Preceding each test, the laser Doppler vibrometer was used to record the mechanical response of the plate under random excitation to identify the resonant frequencies. The H1 frequency response estimators for a sample of 85% solids loading with 0% and 15% additive content in response to three levels of random excitation are presented in Figure 11. Note that the mechanical response of the plate with intentional stress concentrations does exhibit similar trends to the standard plate responses presented previously at the bulk scale explored in this experiment.

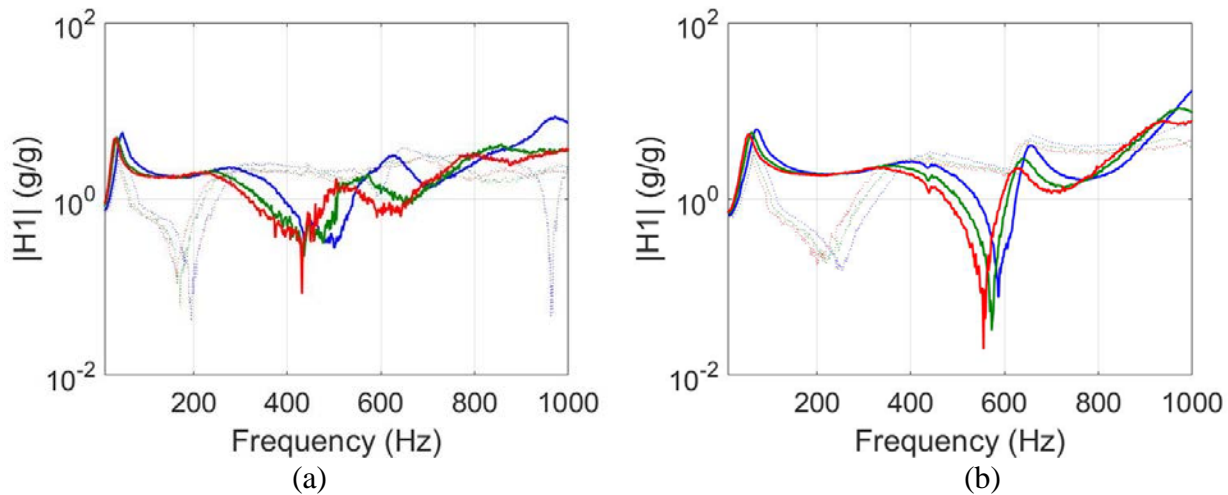


Figure 11. Experimental H1 mechanical frequency response estimator of an (a) 85% solids loading – 0% additive content plate and an (b) 85% solids loading – 15% additive content plate with intentional stress concentrations at three levels of excitation. The red, green, and blue curves depict responses at 2.44, 1.86, and 1 g RMS, respectively. The solid lines represent data obtained from the geometric center, and the dashed lines represent data obtained from an offset point.

In an effort to characterize the local heating near the intentional stress concentrations, the spatial average and maximum temperature increase of the 85% solids loading with 0% and 15% additive content plates over the 60 min window are presented in Figure 12a and 12b, respectively, at the tip of the crack, the circumference of the hole at the top surface, and the step in thickness. The samples were each excited at the respective first resonant frequency. The bulk scale average and maximum temperature increases for the entire surface of the plate are also presented for comparison. In regards to mean temperature, the crack tip exhibits the greatest temperature increase in each formulation. However, the bulk scale temperature increase appears to be greater when analyzing the maximum temperature across the surface of the plate.

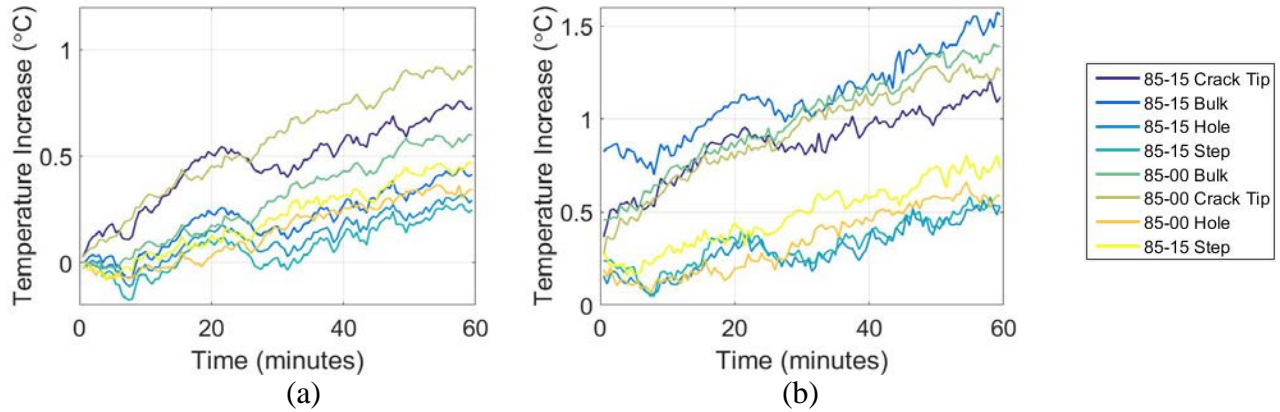


Figure 12. A comparison of the experimentally obtained plate surface temperature versus time in response to a 2 g harmonic excitation near the first resonant frequency for plates of 85% solids loading with 0% additive content and 85% solids loading with 15% additive content. Data is presented for the (a) mean and (b) maximum plate surface temperature versus time. The legend indicates the plate sample tested for each profile, and the physical location on the top surface of the plate.

4.1.3 The Effect of Insulated Boundary Condition

In addition to the tests described above, the thermal behavior of representative samples in response to a 2 g sinusoidal excitation at resonance was recorded under insulated boundary conditions for the plate samples with minimum and maximum additive content of the new PBXN-109 formulation. These plates were comprised of 85% solids loading (15% HTPB binder), with 0% and 30% spherical aluminum powder relative to the weight percent of sucrose. The spatial average and maximum surface temperature increases are given below in Table 3. Ambient temperature increases from previous experiments are included for comparison. The insulated boundary condition exhibited greater heat generation as expected.

Table 3: A comparison of the mean and maximum temperature increase under ambient and insulated thermal boundary conditions for the minimum and maximum additive content samples.

Solids Loading- Additive Content- Sample	Mean Surface Temperature Increase (°C)		Maximum Surface Temperature Increase (°C)	
	Convective	Insulated	Convective	Insulated
85-00-01	0.52	1.26	0.90	1.51
85-30-01	0.81	1.60	0.97	1.77

In order to model the experimental temperature responses outlined above, a thermal simulation was performed with a commercial finite element package using convective and insulated conditions. The theory and assumptions used to model the simulation are outlined in Miller et al. [3] in which the heat source is given by

$$r_{avg} = \frac{\omega}{2\pi} \int_{t_0}^{t_0 + \frac{2\pi}{\omega}} \sigma \frac{\partial \epsilon}{\partial \tau} d\tau = \pi_0(\eta\omega) \quad (25)$$

where η is the loss factor, ω is the frequency of excitation, and π_0 is the strain energy density given by

$$\pi_0 = \frac{E' \epsilon_0^2}{2(1 - \nu^2)} \quad (26)$$

where E' is the real part of the dynamic modulus of the plate, ν is Poisson's ratio, and ϵ_0 is the strain magnitude. The dynamic modulus was obtained using a system identification approach developed by Paripovic [18]. Specifically, the technique used acceleration data from uniaxial compression tests to estimate the stiffness and damping coefficients, which are then used to identify dynamic mechanical properties. Transient thermal properties for each representative plate were determined using the transient plane source technique [26]. The dynamic modulus (E'), thermal conductivity (k), and thermal diffusivity (α) were measured as 3.02 MPa, 0.35 W/(m-K), and 2.84×10^{-7} m²/s, respectively, for a representative plate of 85% solids loading with 0% additive content. The density of 1250 kg/m³ was taken as the average of the two 85-00 plate sample densities, and the structural loss factor of 0.41 was estimated as the inverse of the experimental quality factors for the two 85-00 plate samples.

The thermal behavior for a representative plate of the minimum additive content formulation was simulated in response to the heat source in Equation 25. Convective simulations assumed insulated clamped ends with convective boundary conditions on all of the other surfaces. Insulated boundary condition simulations assumed all of the surfaces to be perfectly insulated. The transient average and maximum temperature response for a representative plate of 85% solids loading with 0% additive content over the 60 min time period is presented as Figure 13a and 13b. Note that the assumption of perfectly insulated plate boundaries provides an upper bound of temperature increase for the experimental results presented above. As expected, the insulated surface assumption results in significantly greater temperature rise than the convective condition.

Interestingly, the thermal simulation under-predicts the temperature increase in both mean and maximum surface temperature for the simulated 85-00 plate, evident by the comparison of the first row of Table 3 with the final magnitude of the curves in Figure 13. This suggests the potential presence of particle-scale interactions that are not accounted for in the derivation of the simulation, such as friction between particles or de-bonding of the particle-binder interface [24,27].

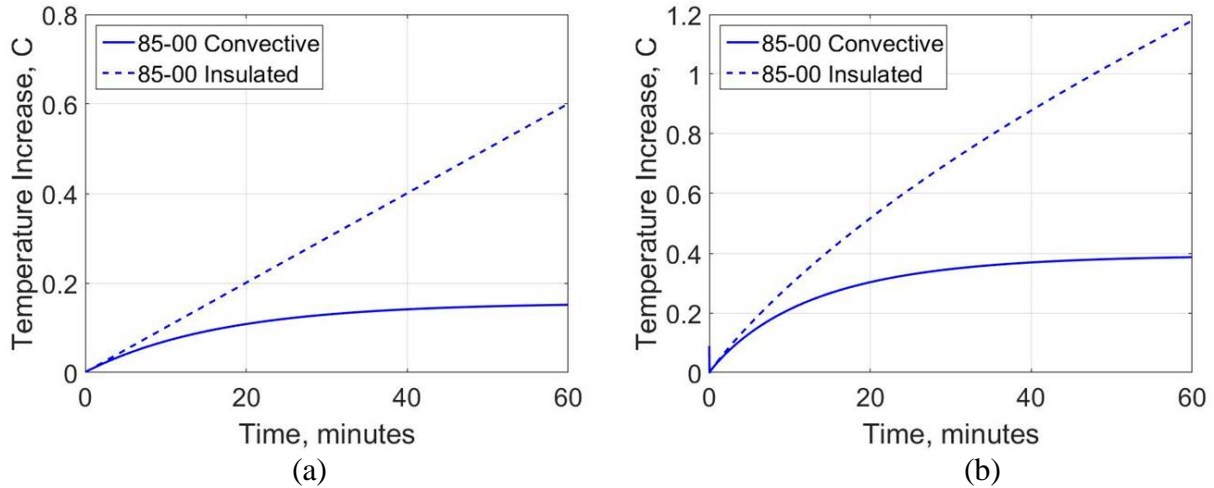


Figure 13. Numerically simulated plate surface temperatures versus time in response to a 2 g excitation near the first resonant frequency for a representative plate of 85% solids loading with 0% additive content. Data are presented for the (a) mean and (b) maximum plate surface temperatures versus time.

4.2 Dissipative Modeling and Material Property Parameter Estimation

4.2.1 An Exploration of Repeatability

Both same-day and day-to-day repeatability studies on the current PBXN-109 (mock) sample set are of interest. Sample repeatability results obtained under both the random and swept sine base excitation are shown in Figures 14 and 15 respectively.

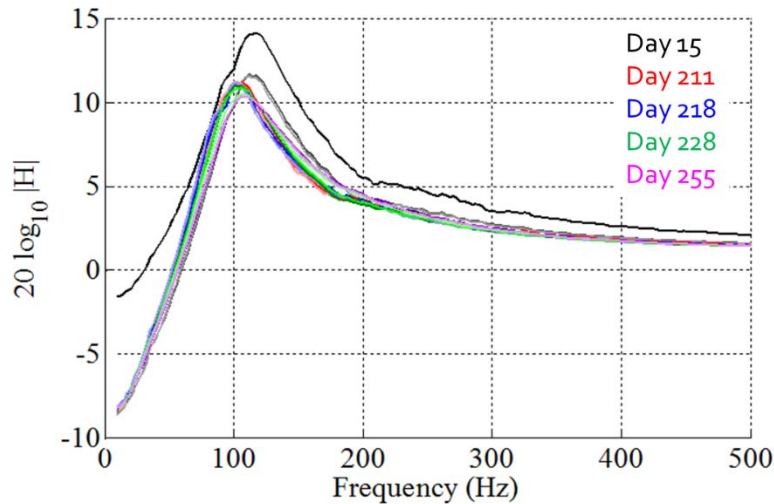


Figure 14. The magnitude of the frequency responses estimates generated from random base excitation tests on P85 S100 A00. The excitation power spectral density was set at $0.025 \text{ g}^2/\text{Hz}$. The spectral resolution is 0.73 Hz. A Hann window with 50% overlap was used in estimation with 143 segments averaged. Each color represents results from a different day of testing.

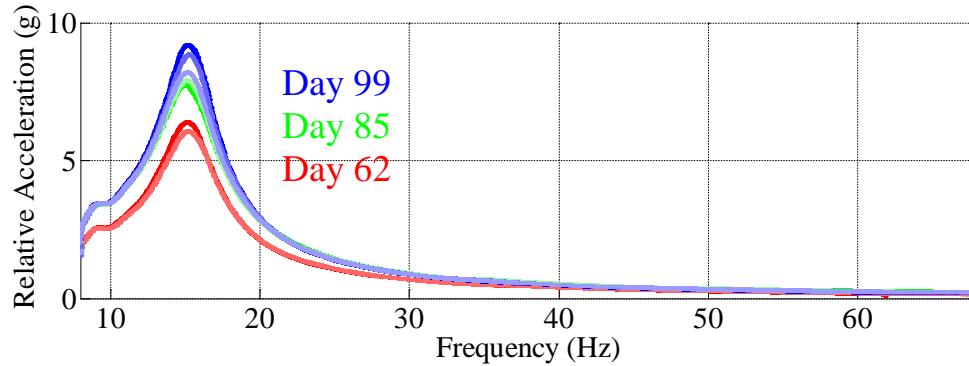


Figure 15. The relative acceleration envelope results obtained from P00 Q000 Q00 C03. The sample was excited at 5 g base excitation from 8 Hz to 68 Hz for 60 s at 1 Hz/s. Each color represents results from a different day of testing. The shading are different tests on the same day from dark to light.

The results obtained from random base excitation tests conducted on the same day on the P85 S100 A00 sample (Figure 14) are very close to one another. There is a change in results between the first and second test on day 15, but for the tests on all of the other days the estimated frequency response magnitudes are very close to each other. The peak in the frequency response magnitude shifts from 118 Hz to 105 Hz, a 13 Hz shift to a lower frequency location. This could be attributable to an increase in damping, softening behavior, or a combination of both.

Similarly, the results of the swept sine base excitation tests conducted on the same day on P00 Q000 Q00 C03 (Figure 15) are very close to one another. There is a change in results between the first and second test on day 62 and on day 92. The resonance frequency remains near 16 Hz; however, the amplitude of the response increases from 6.5 g to 9.1 g.

For both of these samples, and for several of the other samples that have been tested, occasionally the results of the first test on a day are different for results from the second and third test on the same day.

4.2.2 The Effects of Additives

We have also investigated the effects of having the aluminum additive in the sample composition, as well as the geometry of the sample. Random base excitation tests were conducted on P00 Q000 Q00 (pure binder), P85 S100 Q00 (85% sugar solids), and P85 S070 A30 (59.5% sugar solids and 25.5% aluminum additive solids) for both 3 in tall/diameter and 1 in tall/diameter samples. The estimates of the coherence and the magnitude of the frequency response function ($|H|$) for the 6 different samples are shown in Figure 16. Note that only the last trial for each test is shown for clarity, the same day trials for the samples are very similar, indicative of good same day repeatability. The binder only samples are much softer than the binder-crystal combinations, hence the much lower resonance frequency for the binder (red curves in Figure 16). The added mass for the large samples is 2.73 kg (mass/unit area = 598 kg/m²) and for the smaller samples is 1.07 kg (mass/unit area = 1939 kg/m²).

For the larger cylinders [Figure 16a] the coherence remains near unity for all three sample compositions with small dips near resonance and twice the resonance. However, for the smaller samples, the results for the high solids loading with only sugar sample (green - P85 S100 Q00) show a very low coherence from 10 Hz to 300 Hz particularly close to twice the resonance frequency, which is indicative of high degrees of quadratic nonlinearity, but this is not observed with the other small sample where the solids are 70% sugar and 30% aluminum. However, the frequency response magnitudes for samples with the high solid loading with aluminum additive content (blue) exhibit two peaks and there is evidence of some nonlinearity, but it is much weaker than for the sugar only samples. The cause of the double peak is under investigation. The peaks are closer together in the larger sample frequency response [Figure 16a] than seen in the smaller sample frequency response [Figure 16b]. All of these features suggest that it is important to include nonlinear terms in the models for these samples with high solids loading. The behavior of the binder indicates that at these excitation levels, the behavior is close to being linear. We are continuing testing on these samples, as well as new samples of the same composition, to continue to build our understanding of the repeatability of tests on these materials and how the samples' behaviors may change as the materials age. Due to fracturing of the sample, we are yet to repeat the test on a 1 in tall/diameter P85 S100 Q00 sample. In the near future, we will conduct the test on a sample of the same geometry and composition to investigate how the response changes with testing duration.

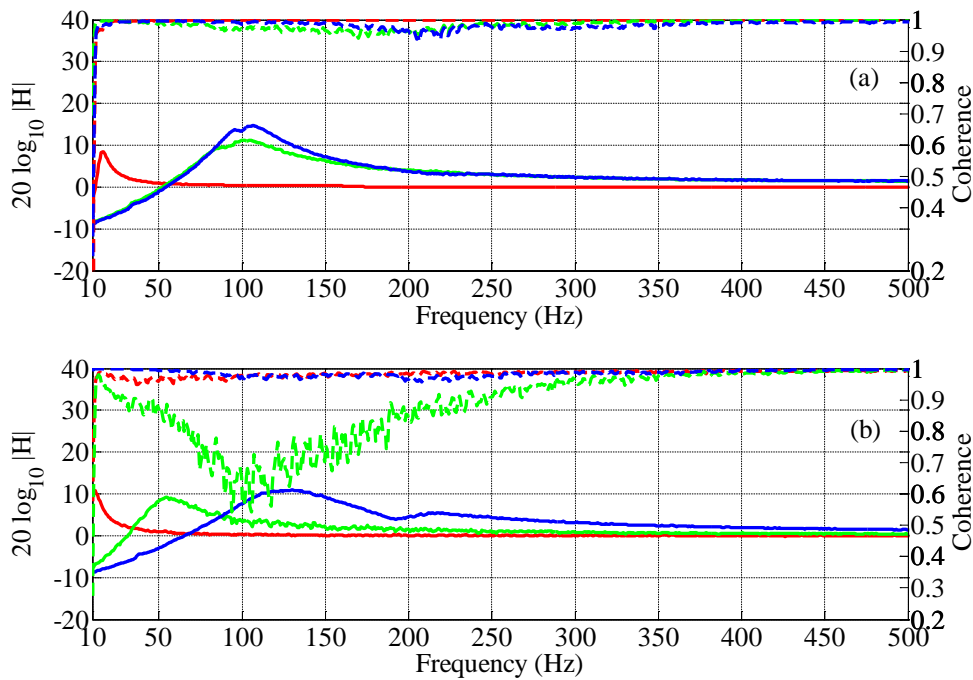


Figure 16. Results from random base excitation for the PBXN-109 formulated (mock) samples excited for 100 s from 10 Hz to 1000 Hz at 0.025 g²/Hz. Solid lines denote the estimated magnitude of H and the dashed line denotes its respective coherence. Red denotes results for sample P00 Q000 Q00 C0#, green is for P85 S100 Q00 C0#, and blue is for P85 S070 A30 C0# for (a) large cylinders (3 in tall/diameter) and (b) small cylinders (1 in tall/diameter).

4.2.3 Model Order, Stability, and Convergence Improvement

The parameter estimation code has been improved over previous versions by adjusting the convergence criteria so that now it converges faster to the viscoelastic parameter estimates. Parameters estimates for the P85 S070 A30 sample were generated using a model with a linear viscous damping term, a fifth order polynomial stiffness, and various viscoelastic kernel orders. In this model the viscoelastic term is a convolution of the relaxation kernel and the relative velocity response \dot{z} . Thus, the model is of the form:

$$m\ddot{z}(t) + c\dot{z} + \sum_{i=1}^5 k_i z^i + \int_{-\infty}^t \dot{z}(\tau) \sum_{i=1}^M \beta_i e^{-\alpha_i(t-\tau)} d\tau = -m\ddot{y} \quad (27)$$

The viscoelastic kernel order M was varied from 10 to 60 in steps of 10. The viscoelastic kernel is denoted by $g(t)$ and the corresponding viscoelastic term frequency response is denoted by $G(f)$. The estimates of $G(f)$ for various model orders are shown in Figure 17. The threshold where there appears to be a sufficient number of terms in the kernel to model the viscoelastic behavior accurately is $M = 40$. The blue line in the plot is the estimate of $|G(f)|$ derived after the first part of the iterative estimation procedure where the estimates of c and k_i ; $i = 1, 2, \dots, 5$ are updated. Note that the blue line is the converged estimated of $|G(f)|$ from the model where $M = 60$.

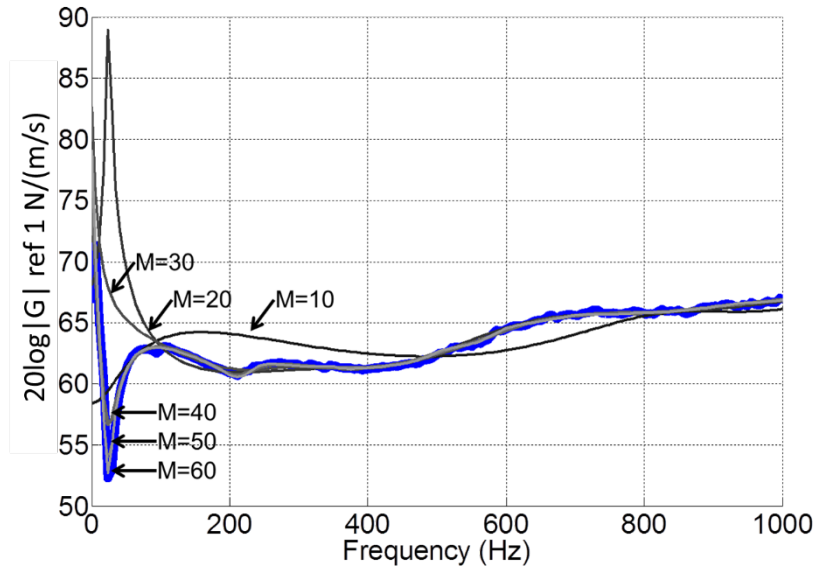


Figure 17. The magnitude of the viscoelastic kernel frequency response derived by fitting the nonlinear viscoelastic model to data from the random base excitation test on P85 S070 A30. The blue line is the G response of the viscoelastic term. The black and gray lines are of the different fits for M varying from 10 to 60 in 10 step increments.

When fitting a higher order viscoelastic model (model order is greater than 20) to the frequency response of a randomly excited mock energetic sample, an unstable model is often estimated. In the estimation the viscoelastic transfer function is modeled as a digital filter, and it being unstable means that at least one pole is outside the unit circle in the z -plane. This is problematic because the filter is used to predict the viscoelastic term for use in the next stage of the algorithm. To deal

with this problem, the terms associated with the unstable poles are removed and a reduced order viscoelastic transfer function is calculated before continuing with the next step in the iterative estimation process.

An example result from a base excitation test on a pure binder sample (P00 Q000 Q00) with random excitation applied in the 10 to 1000 Hz frequency range at $0.025 \text{ g}^2/\text{Hz}$ is shown in Figure 18. The estimated viscoelastic frequency response generated by using the relative velocity and the viscoelastic fit from the previous step in the algorithm (red line) and the estimated digital filter frequency response at the end of this step (green line) for iterations 1, 20, 60, 120, and 180 are shown. After 60 iterations the estimated digital filter's frequency response function is a good fit to the frequency response function estimated from the time histories generated in the previous step. After 180 iterations the fit is very good.

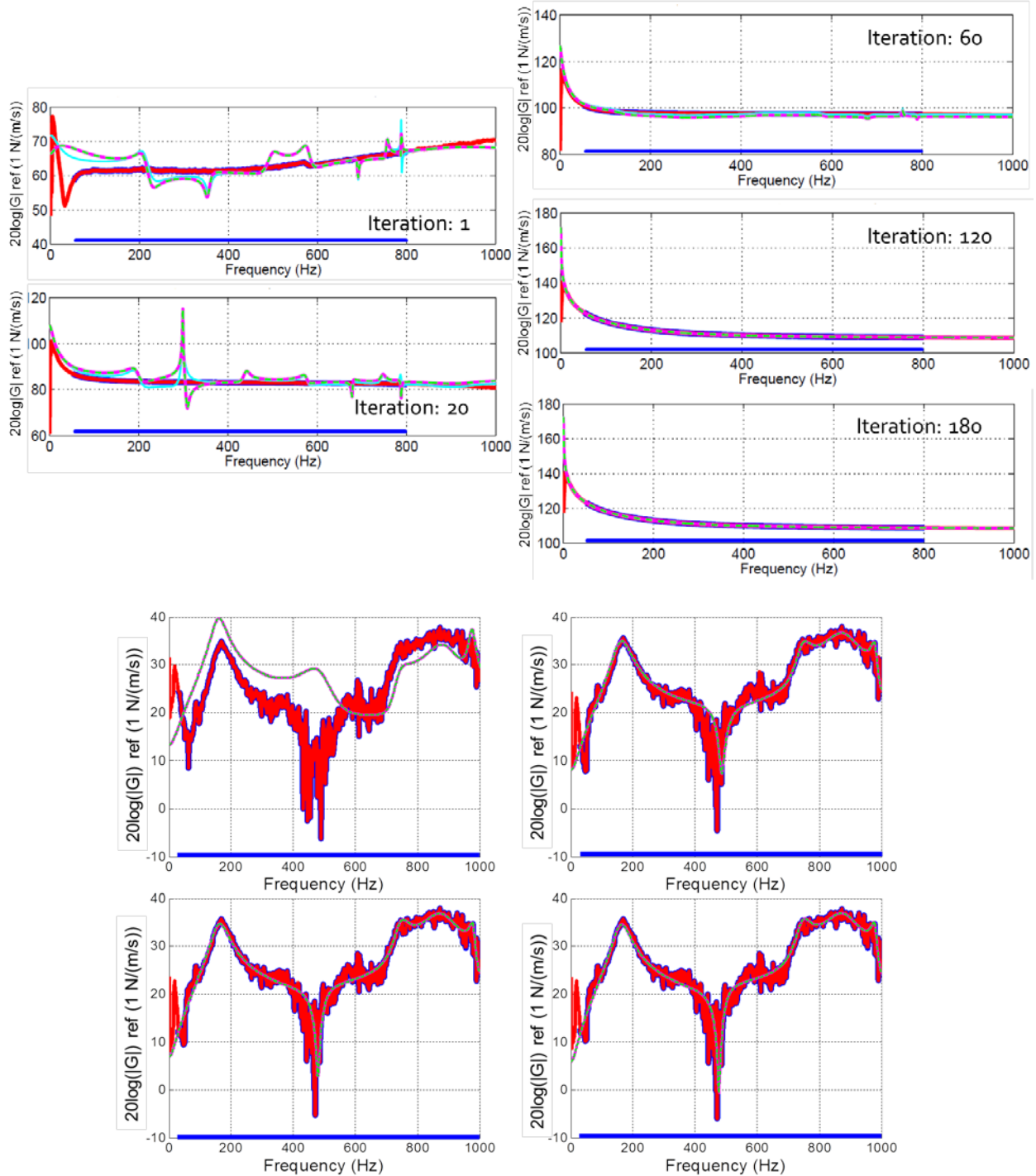


Figure 18. The magnitude of the viscoelastic frequency response estimates of sample P00 Q000 Q00 at various stages in the iterative system identification process. The results of H1 estimation from the time histories generated in the previous step in the algorithm are shown by the red line, and the estimated digital filter's frequency response is the green line. Results are shown for iterations: 1, 20, 60, 120, and 180. The blue line defines which portion of the H1 estimate of the frequency response function (red) was used in the estimation process [$f = \dot{z}$, $M_1 = 40$, $M = 20$].

Currently, we are still working on the modeling component of this task. When applying the iterative estimation technique to experimental data (high solids loading) when $\lambda > 0$ we observe convergence issues for higher order models ($M > 20$). The parameter estimation method was applied to the response of a randomly excited high solids loading sample, P85 S085 A15 (85% solids, where 85% of the solids are sugar and 15% are aluminum additive). This time the c estimate did not converge, rather the c estimate continued to decrease with each iteration number. This was balanced by the viscoelastic frequency response fit level continually increasing with each iteration. The damping term may be competing with the viscoelastic components and as one increases the other decreases to compensate. This may mean that a viscoelastic term may not be needed at all, or that for materials with very high solids loading it may need to take a different form.

Further clarification of the stability challenges that arise, the iterative approach, and how the instability is handled is described below. Recall that the parameter estimation approach may be described by the flowchart shown in Figure 19 (Please refer to [11] for additional details).

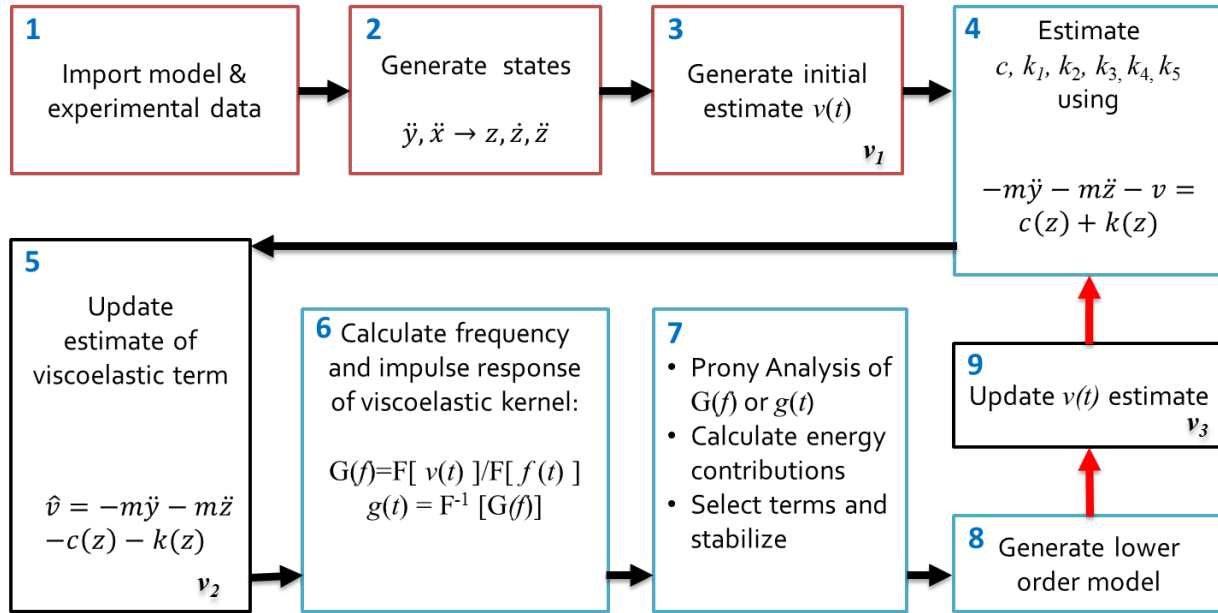


Figure 19. The steps in the iterative parameter estimation approach

When the viscoelastic kernel is estimated for a second time in the iterative loop, some of the estimated terms may be unstable. To avoid this, steps are taken to ensure that stable filters are created. Recall that the relaxation kernel within the viscoelastic term is of the form:

$$g(t) = \sum_{i=1}^M \beta_i e^{-\alpha_i t} \quad (28)$$

We can rewrite Equation 28 in the discrete time domain (where $t=n\Delta$),

$$g(n\Delta) = \sum_{i=1}^M \Delta \beta_i e^{-\alpha_i n\Delta} \quad (29)$$

The model of the sampled system transfer function that relates the sampled forcing function to the sampled viscoelastic term ($v_n = v(n\Delta)$) is determined by taking the z -transform of ($g_n = g(n\Delta)$). The transfer function is of the form:

$$G(z) = \sum g_n z^{-n} = \sum_{i=1}^M \frac{\beta_i}{1 - e^{-\alpha_i n \Delta} z^{-1}} \quad (30)$$

where β_i is the residue and $e^{-\alpha_i n \Delta}$ is the pole position. We can combine and rewrite Equation 30, it is of the form:

$$G(z) = \frac{b_0 + b_1 z^{-1} + \dots + b_{M-1} z^{-(M-1)}}{1 + a_1 z^{-1} + \dots + a_M z^{-M}} \quad (31)$$

If we substitute $z = e^{j2\pi\lambda}$ into Equation 31 we can calculate the frequency response of the discrete system. We then use that equation and the frequency response estimate from stage 6 (in the flowchart) to estimate b_i and a_i , (Please refer to [11] for additional details). If we wish to estimate a model of order M , we typically start with an order $M_1 \gg M$ and then select the M strongest contributors to the impulse response. So at this stage we take Equation 31 with $M = M_1$ and the estimates of a_i and b_i and decompose it to be in the form of Equation 30. In the z -plane if the estimated pole is outside of the unit circle, i.e. $|e^{-\alpha_i n \Delta}| > 1$, the filter is unstable. The user has a choice to either remove the unstable pole or reflect the unstable pole back inside the unit circle. These are combined in the form of Equation 31 and the response v_3 is estimated by using the difference equation, which is of the form:

$$v_n = \hat{a}_1 v_{3_{n-1}} - \dots - \hat{a}_M v_{3_{n-M}} + \hat{b}_0 f_n + \dots + \hat{b}_{M-1} f_{n-(M-1)}, \quad (32)$$

where $\hat{\cdot}$ denotes an estimated parameter. This stabilization works well when $\lambda = 0$.

Recently, we have explored the effects of hysteretic damping and found that a refined stabilization method and different filtering approach are needed. This need arose because when calculating \hat{b}_i and \hat{a}_i numerical rounding would cause the viscoelastic poles to drift outside the unit circle creating an unstable filter. The details of the new approach may be found in the August 2017 monthly report. The results shown in this report are for models with $\lambda = 0$, and using the method described above. We are also working on developing an automatic way for the system identification code to determine the model order, including the case of no viscoelastic term, and also investigating the use of different types of damping terms and different viscoelastic forcing terms.

4.2.4 Code Sharing and Other Updates

In this performance period we have compiled a set of 11 standardized user guides and computer codes. The user guides for the programs and function codes includes an example input along with an expected output and how to implement and run the code. In the preamble to the code for a particular function, descriptions of what the function does, the input and output variables, the version number of the code, and, if applicable, a list of what updates have been incorporated since the last version was given. These 11 MATLAB functions feed into each other to allow the user to investigate the different experimental data and create and save a pdf of the data. The flowchart of how these functions are connected is shown in Figure 20.

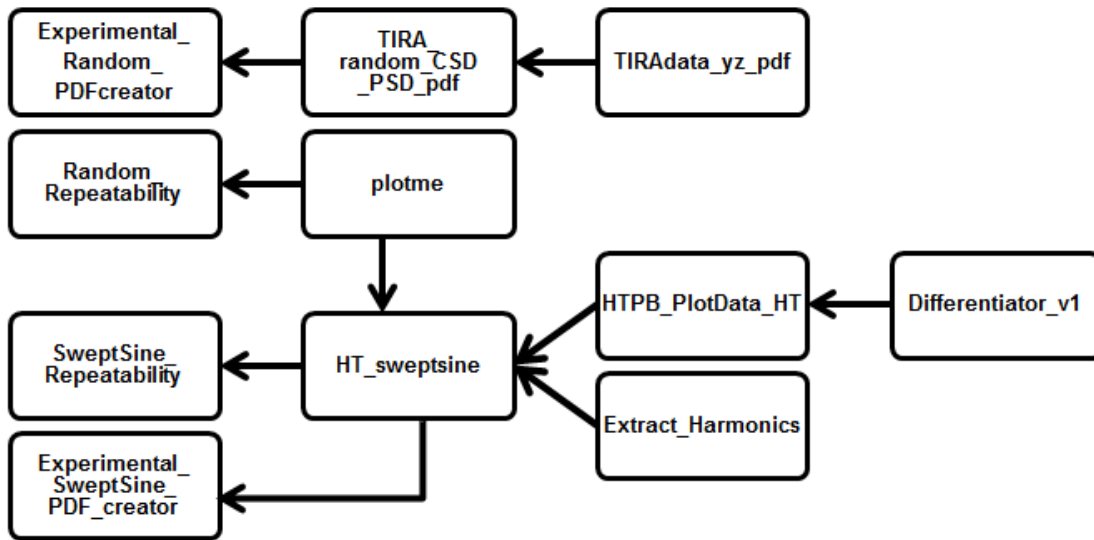


Figure 20. A flow chart of how the 11 functions submitted as part of this report feed into each other to allow the user to investigate the repeatability and experimental set up of the samples

Also, in this performance period we compiled an EXCEL-based user guide to help people navigate and find specific test data in the database that we have developed to store the data from the random and swept sine base excitation tests on the different material samples. The 176 tests conducted on the PBXN-109 (mock) samples are tabulated in a Microsoft Excel spreadsheet that contains the following columns: (A) sample identification number, (B) date name, (C) test date, (D) cure date, (E) age at time of test, (F) diameter (in), (G) height (in), (H) test type, (I) forcing, (J) frequency range, (K) filename. Each column in the spreadsheet may be sorted or down-selected by using the drop down menu in row 1.

As part of this activity we are also updating our codes to make them more user friendly. We are currently still working on improving our parameter estimation code. Once it has been further tested and ready to share, we will generate user guides for all the functions used to estimate the system parameters along with a flowchart similar to Figure 20. We will then share this completed documentation.

4.3 Endochronic Plasticity Model Results

4.3.1 Experimental Results

Compressive cyclic loading experiments were performed on cylindrical specimens of mock energetic materials. Two types of cyclic tests were performed, namely


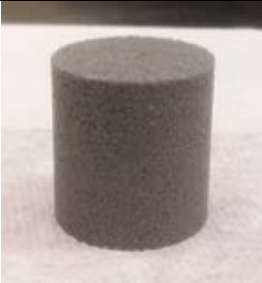
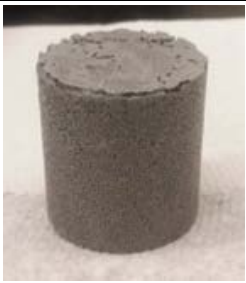
- 1) Cycling between two predetermined strain levels; and
- 2) Cycling between two force levels, with the lower force being close to zero.

While (1) has the advantage of being a well-controlled and repeatable experiment, it may be difficult to utilize it for model calibration. On the other hand, (2) appears to be much more calibration-friendly; however, it is more difficult to control since it is not possible to measure zero force accurately when the loading is unidirectional. To alleviate this problem, data acquisition began after the specimen was subjected to a small preload, and cycling was performed between the preload and the higher force level.

Apart from cyclic loading tests, simple compression tests were also performed to determine the initial loading behavior of the materials.

Table 4 summarizes the details of experiments performed on three different compositions of PBXN-109 (mock) specimens.

Table 4. A summary of the experiments performed on three different PBXN-109 (mock) specimens (# denotes the number of cycles)

Experiment Detail	P85 S100 Q00 CXX	P85 S085 A15 CXX	P85 S070 A30 CXX
Composition	15% HTPB 85 % Sucrose 0% Aluminum	15% HTPB 72.25% Sucrose 12.75% Aluminum	15% HTPB 59.5% Sucrose 25.5% Aluminum
Image			
Dimensions	1 in × 1 in	1 in × 1 in	1 in × 1 in
Type of cyclic force loading	- Sample C05: 1 N – 50 N (#30) - Sample C06: 1 N – 75 N (#30) - Sample C03: 1 N – 125 N (#30) - Sample C04: 1 N – 175 N (#30)	- Sample C03: 1 N – 175 N (#30) - Sample C06: 1 N – 175 N (#35)	- Sample C02: 1 N – 75 N (#40)
Type of cyclic strain loading	N/A	- Sample C00: 10 - 20% (#20) - Sample C01: 1 - 2% (#20)	N/A
Simple compression	- Samples C00, C01 and C08: loaded until an instability was observed	- Sample C02, C04 and C05: 0 - 30%	- Sample C01: 0 - 30%
Strain Rate	0.001 s ⁻¹ for all tests	0.001 s ⁻¹ for all tests	0.001 s ⁻¹ for all tests
Sampling Rate	100 Hz	100 Hz	100 Hz

The energetic material response may be characterized based on the following properties:

- Specimen Composition
- Specimen Age
- Specimen-to-specimen variability

The following sections provide an analysis of the experimental observations based on the above characteristics.

Effect of Age and Variability among Specimens

Figure 21 shows the simple compression results for P85 S100 Q00 CXX samples. Figure 21a provides the simple compression stress-strain responses for samples aged 10, 19 and 26 days respectively. The trend of stress-strain evolution was consistent among the three samples, each of them showing a nonlinear increase in stiffness until about 4% deformation, followed by a decrease in stiffness until an instability (near zero stiffness) was observed. In addition, an apparent trend of

increasing stiffness is observed with aging. Figure 21b shows the configuration of sample P85 S100 Q00 C00 at about 7% deformation, whereat an instability was observed in the response.

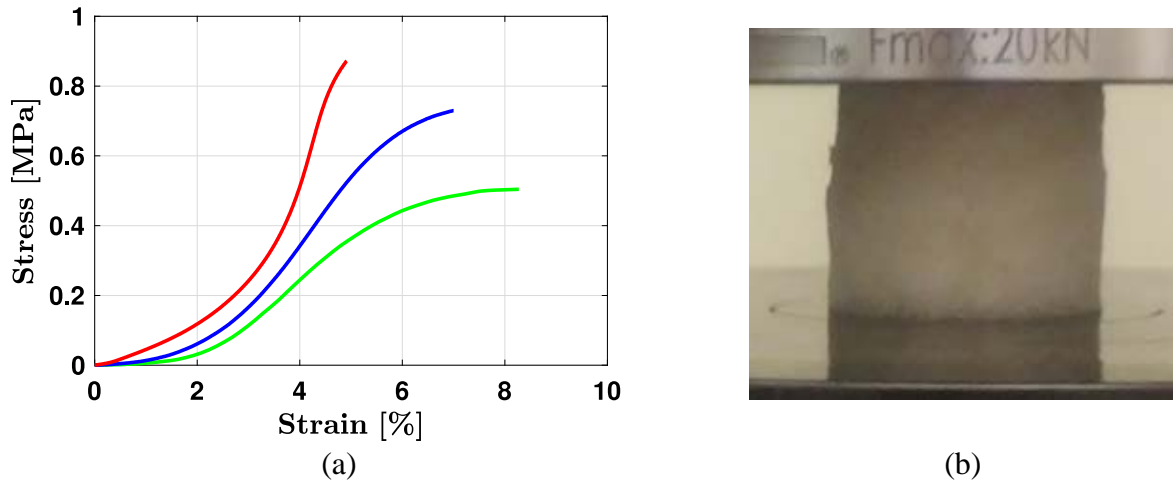


Figure 21. (a) Simple compression stress-strain responses of P85 S100 Q00 C00 (green curve, aged 10 days), P85 S100 Q00 C01 (blue curve, aged 19 days) and P85 S100 Q00 C08 (red curve, aged 26 days). (b) Configuration of P85 S100 Q00 C00 specimen at 7% deformation.

Figure 22 provides the cyclic loading responses for P85 S100 Q00 CXX specimens, compared with the simple compression curves in Figure 21a. In this and all subsequent figures, the cycles are represented by a spectral color map ranging from red (1st Cycle) to blue (Stabilized Cycle). Ideally, coeval specimens should have similar stress-strain responses, meaning that the initial loading curve of the cyclic response of a specimen must be close to the simple compression curve of a coeval specimen. For all of the specimens presented in Figure 22, the coeval specimen from Figure 21 is P85 S100 Q00 C01.

The plots in Figure 22 show that although the initial loading curves of specimens P85 S100 Q00 C03 and P85 S100 Q00 C04 are somewhat close to the compression curve of P85 S100 Q00 C01, the same is not true for specimens P85 S100 Q00 C05 and P85 S100 Q00 C06. This observation may be attributed to the presence of specimen-to-specimen variations in the form of micro-defects, surface texture, pore density etc.

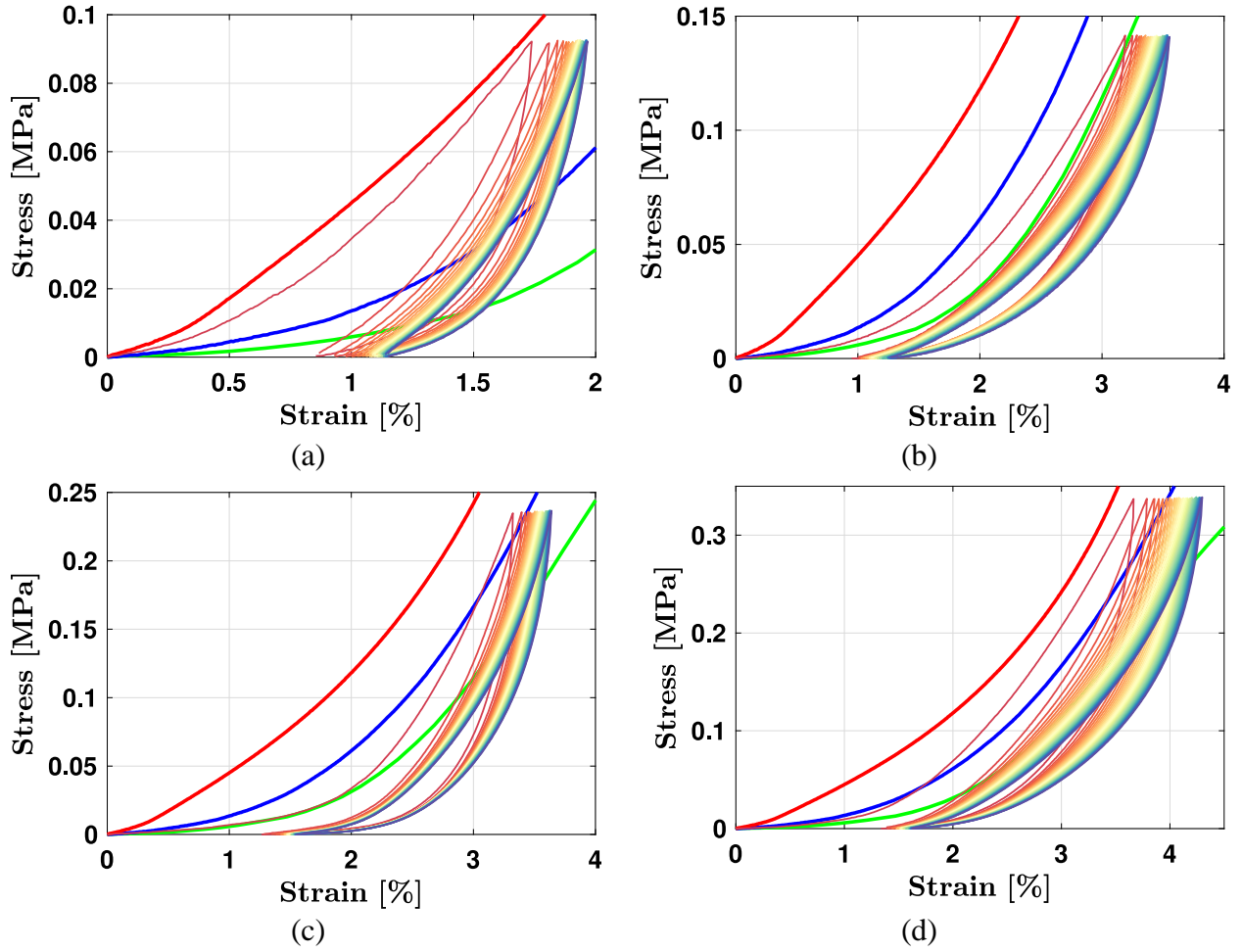


Figure 22. Cyclic compressive stress-strain responses of (a) P85 S100 Q00 C05 (peak load 50 N, aged 19 days), (b) P85 S100 Q00 C06 (peak load 75 N, aged 21 days), (c) P85 S100 Q00 C03 (peak load 125 N, aged 19 days), and (d) P85 S100 Q00 C04 (peak load 175 N, aged 19 days), compared with the three simple compression curves from Figure 21a.

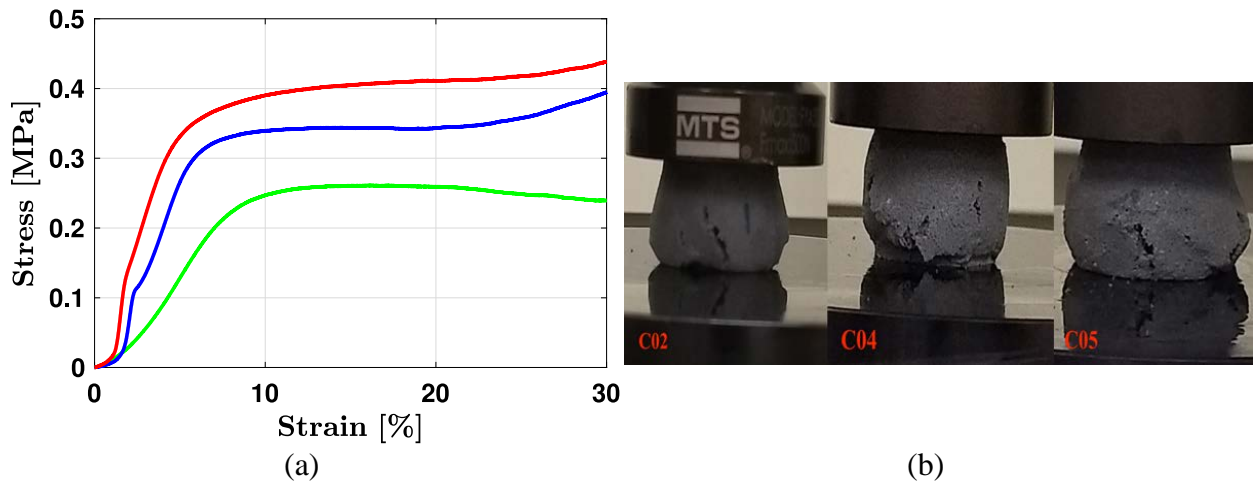


Figure 23. (a) Simple compression stress-strain responses of P85 S085 A15 C02 (red curve, aged 1 day), P85 S085 A15 C04 (blue curve, aged 6 days) and P85 S085 A15 C05 (green curve, aged 6 days). (b) Configurations of the three tested specimens at 30% deformation.

Figure 23a shows the simple compression plots of aged P85 S085 A15 CXX specimens. Interestingly, an opposite trend of decreasing stiffness with age is observed for these specimens as compared to P85 S100 Q00 CXX specimens. Another interesting observation is regarding the behavior of two specimens, P85 S085 A15 C04 and P85 S085 A15 C05. Despite being coeval, C05 has a much smaller stiffness and visibly different stress evolution as compared to C04, suggesting the presence of significant specimen-to-specimen variations.

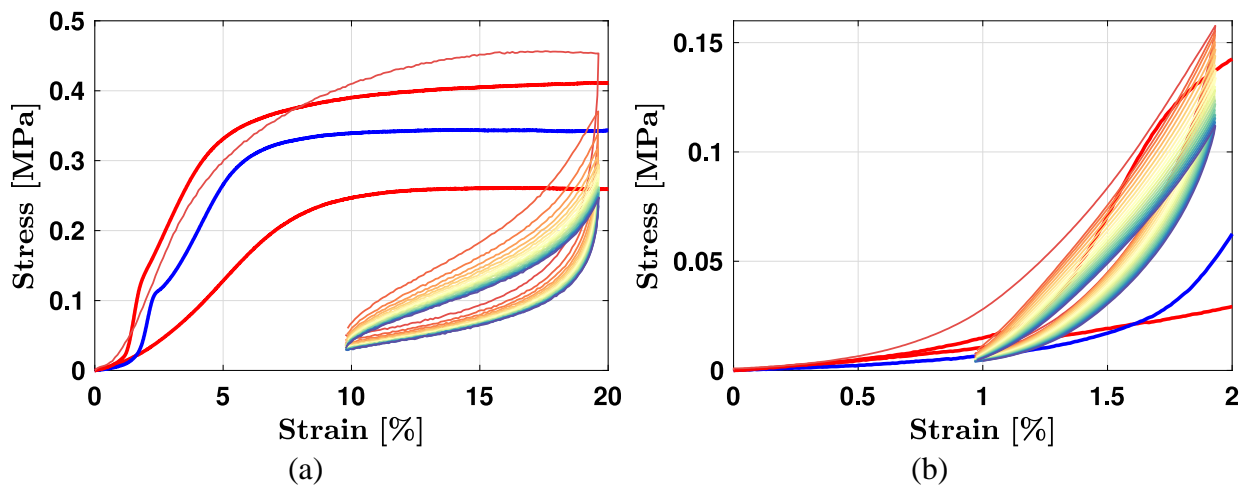


Figure 24. Cyclic compressive stress-strain responses of (a) P85 S085 A15 C00 (strain cycling between 10% - 20%, aged 15 days) and (b) P85 S085 A15 C01 (strain cycling between 1% - 2%, aged 9 days), compared with the three simple compression curves from Figure 23a.

Figure 24 shows the stress-strain responses of cycling between two strain levels for P85 S085 A15 CXX specimens compared with the simple compression curves, with Figure 24a showing the results for C00 specimen, aged 15 days, cycled between 10% and 20% strain, and Figure 24b

showing the same for C01 specimen, aged 9 days, cycled between 1% and 2% strain. In both the figures, the initial loading curve is closer to the compression curve for C02 sample, aged 1 day. From these observations, it may be concluded that the specimen-to-specimen variations are equally, if not more, influential compared to age in characterizing the energetic material response.

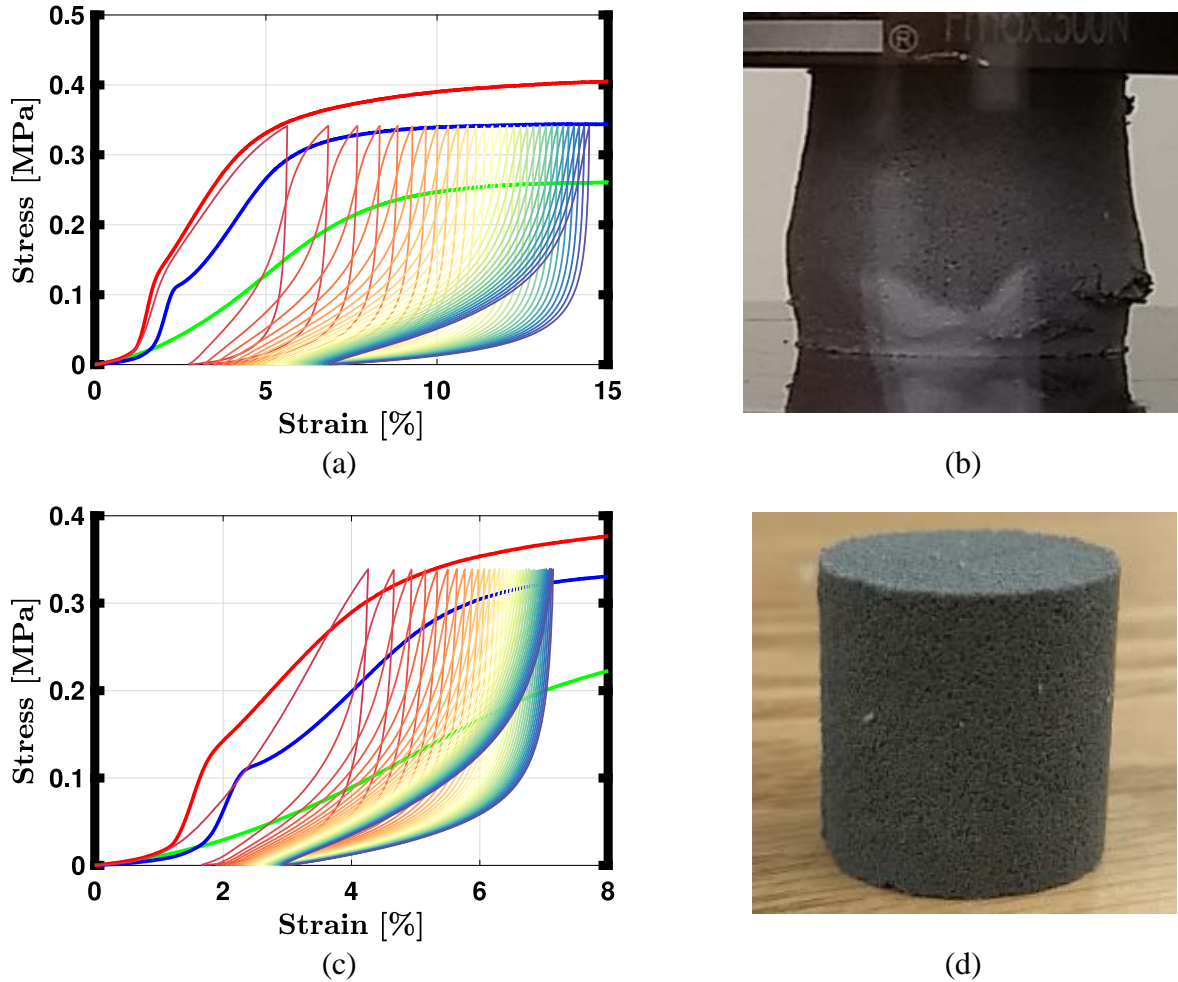


Figure 25. Cyclic compressive stress-strain responses of (a) P85 S085 A15 C03 (peak load 175 N, aged 1 day) and (c) P85 S085 A15 C06 (peak load 175 N, aged 6 days), compared with the three simple compression curves from Figure 21a. Subfigures (b) and (d) represent the final configuration of the samples after completing the tests shown by (a) and (c) respectively.

Observations supporting the above conclusion were also made in Figures 25a and 25c, depicting the cyclic stress-strain responses for two samples P85 S085 A15 C03 and P85 S085 A15 C06, aged 1 day and 6 days respectively. Both samples were cycled between 1 N (Preload) and 175 N force levels, for 35 cycles. However, a significant difference in the stress-strain response of the two specimens was observed. The initial loading response of specimen C03 was very close to the simple compression curve of coeval specimen C02, with stiffness almost the same. On the other hand, the initial loading response of specimen C06 was close to coeval specimen C05 but with much higher stiffness. In addition, specimen C03 underwent significant plastic deformation as compared to specimen C06, which is evident from their configurations after the test, depicted in

Figures 25b and 25d respectively. Irreversible deformations and cracks can be easily observed in C03, while C06 shows almost no signs of visible plastic deformation.

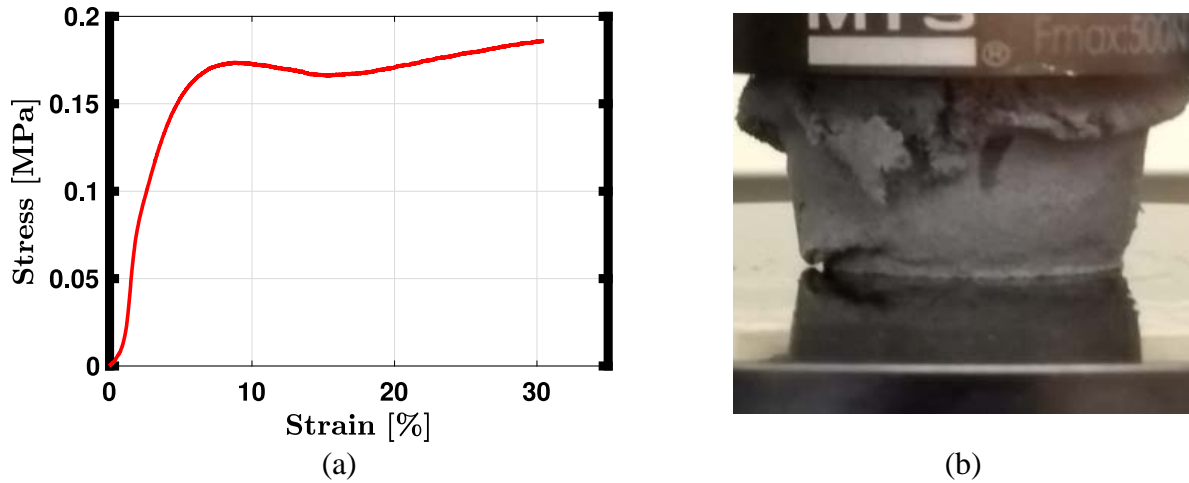


Figure 26. (a) Simple compression stress-strain response of P85 S070 A30 C01 (red curve, aged 6 days). (b) Configuration of the specimen at 30% deformation.

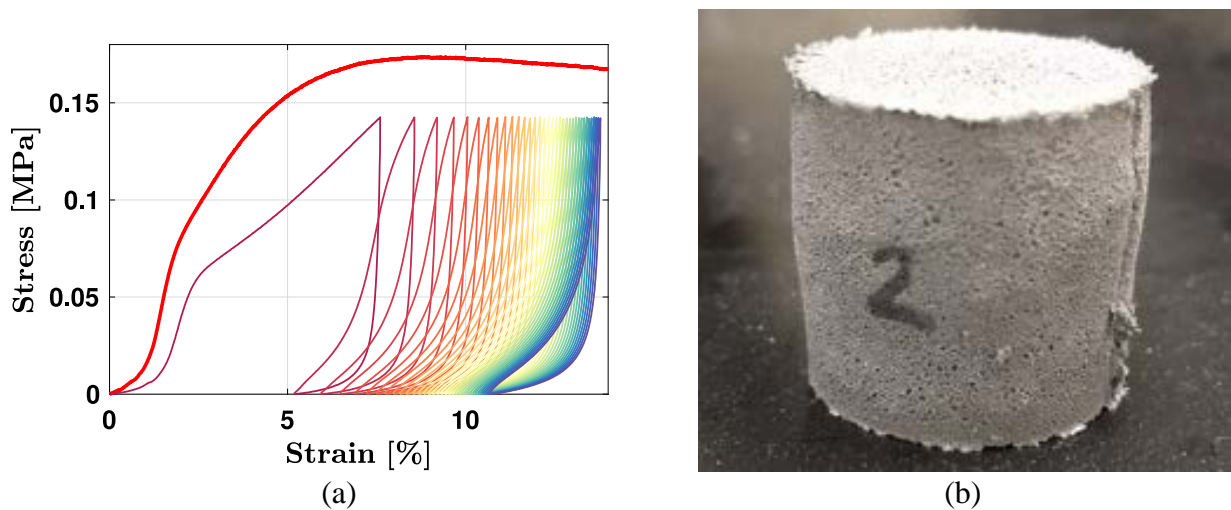


Figure 27. Cyclic compressive stress-strain response of (a) P85 S070 A30 C02 (peak load 75 N, aged 6 days), compared with the simple compression curve of P85 S070 A30 C01 from Figure 26a. Subfigure (b) represents the final configuration of the sample after completing the test.

Figures 26 and 27 present the experimental results of compressive tests performed on P85 S070 A30 CXX specimens. The simple compression response of P85 S070 A30 C01 sample depicted in Figure 26a looks similar to the responses of specimens P85 S085 A15 C02 and P85 S085 A15 C04 in Figure 23a, although with much smaller slope (stiffness) and strength. The initial loading response of the cyclic curve for specimen P85 S070 A30 C02 presented in Figure 27a is roughly similar to the compression curve of coeval specimen P85 S070 A30 C01, however smaller stiffness indicates the presence of specimen-to-specimen variations.

Effect of Specimen Composition

The simple compression plots of mock energetic specimens provided in the previous section show a noticeable variability in the range of stress at the occurrence of instability, marked by sudden significant loss of stiffness, amongst specimens of different composition. For better clarity, the approximate effective stress at instability is plotted against specimen aluminum content in Figure 28. From the figure, it can be easily concluded that the strength of mock energetic material decreases with increase in aluminum content.

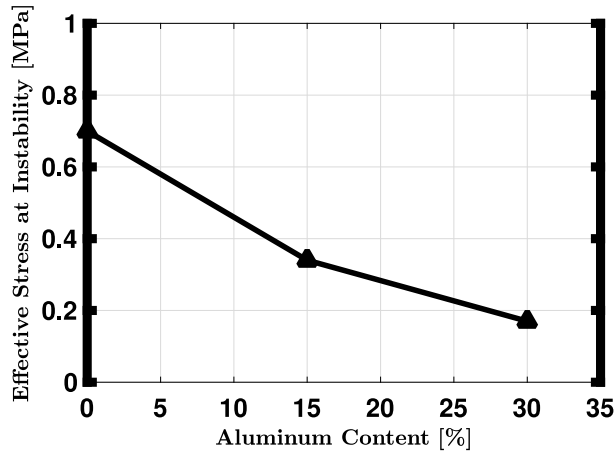


Figure 28. Effective stress at instability vs. aluminum content for the mock energetic specimens

4.3.2 Calibration Procedure, Preliminary Results, Discussion and Future Work

In the Section 3.4.1, we have seen that the finite-strain formulation consists of various material parameters that need to be determined empirically. These parameters are:

- Ogden's model parameters: μ_k and α_k ($k = 1, 2 \dots M$)
- Kernel function parameters: C_j and γ_j ($j = 1, 2 \dots N$)
- Material function parameters: c_m , s_m , $\beta_{1,m}$ and $\beta_{2,m}$ ($m = 1, 2 \dots K$)

Thus, we have $(2M + 2N + 4K)$ empirically determined material parameters. An efficient calibration strategy is essential for the determination of these parameters.

Calibration Procedure

An optimization problem based on the least squares method, similar to the one presented for the small-strain formulation [11], is proposed for model calibration. The problem aims to minimize two objective functions $F_1(\boldsymbol{\theta}_1)$ and $F_2(\boldsymbol{\theta}_2)$, defined as

$$F_1(\boldsymbol{\theta}_1) = \sum_{r=1}^P w_r^1 [\sigma(\boldsymbol{\theta}_1, \epsilon_{exp,r}^1) - \sigma_{exp,r}^1]^2 \quad (33)$$

and

$$F_2(\boldsymbol{\theta}_2) = \sum_{q=1}^R w_q^2 [\sigma(\boldsymbol{\theta}_2, \epsilon_{exp,q}^1) - \sigma_{exp,q}^1]^2 \quad (34)$$

where $\boldsymbol{\theta}_1 = [\mu_k, \alpha_k, C_j, \gamma_j]^T$ and $\boldsymbol{\theta}_2 = [c_m, s_m, \beta_{1,m}, \beta_{2,m}]^T$ are the two vectors comprising of the unknown parameters, with $\boldsymbol{\theta}_1$ holding the Ogden and kernel parameters and $\boldsymbol{\theta}_2$ holding the material function parameters, $[\epsilon_{exp}^1, \sigma_{exp}^1]$ and $[\epsilon_{exp}^2, \sigma_{exp}^2]$ are the experimental datasets corresponding to $\boldsymbol{\theta}_1$ and $\boldsymbol{\theta}_2$ respectively, and w_r^1 and w_q^2 are the respective weights.

To make the optimization problem more efficient, data set 1, i.e. $[\epsilon_{exp}^1, \sigma_{exp}^1]$ comprises of data points for only the first load-unload curve, which is sufficient enough to calibrate the elasticity and kernel parameters. However, data set 2, i.e. $[\epsilon_{exp}^2, \sigma_{exp}^2]$ comprises of the complete stress-strain curve to capture the evolution of $f(z)$.

The two objective functions are minimized simultaneously using a stagger algorithm [11] presented in Figure 29.

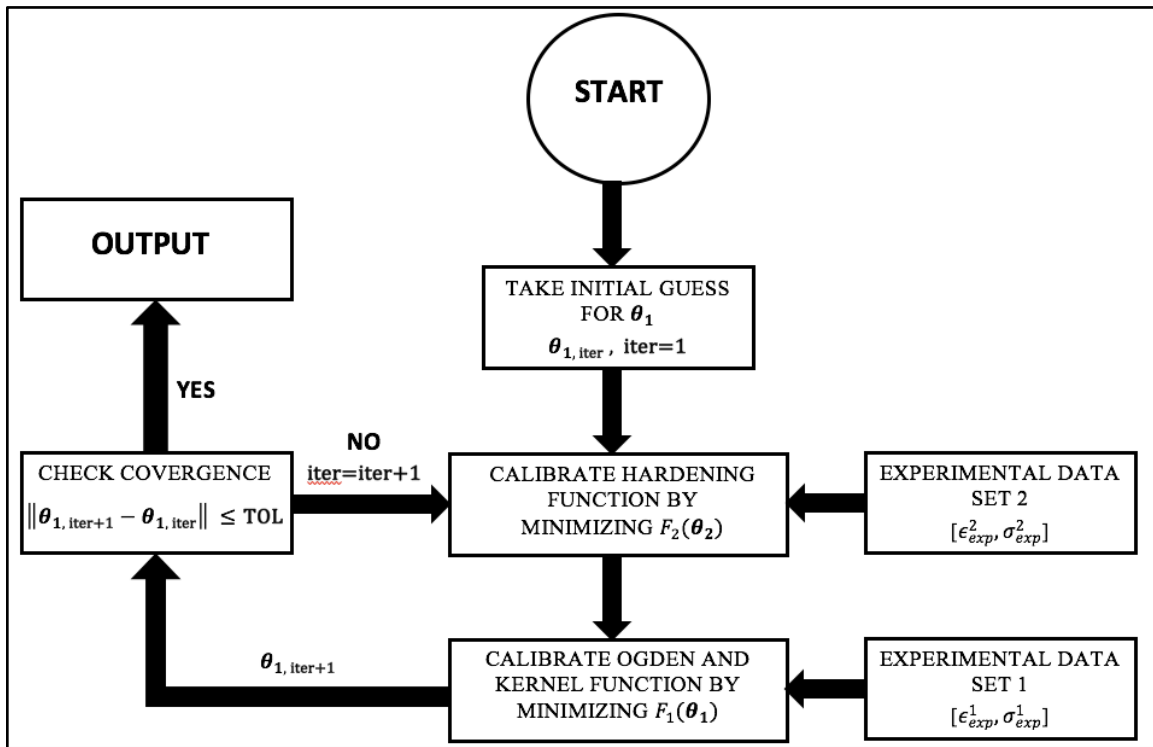


Figure 29. Stagger algorithm for finite-strain model calibration

The complete optimization problem is solved using an in-house MATLAB code based on the in-built minimization function *fmincon*.

Preliminary Results

The calibration procedure was used to calibrate the strain cycling experiment performed on the Pure HTPB Binder (see Figure 5) and P85 S085 A15 C00 (see Figure 24a) specimens. Figure 30 provides the calibration results, and the calibrated parameter values are provided in Table 5. The results show that the model is capable of fairly representing the experimental data.

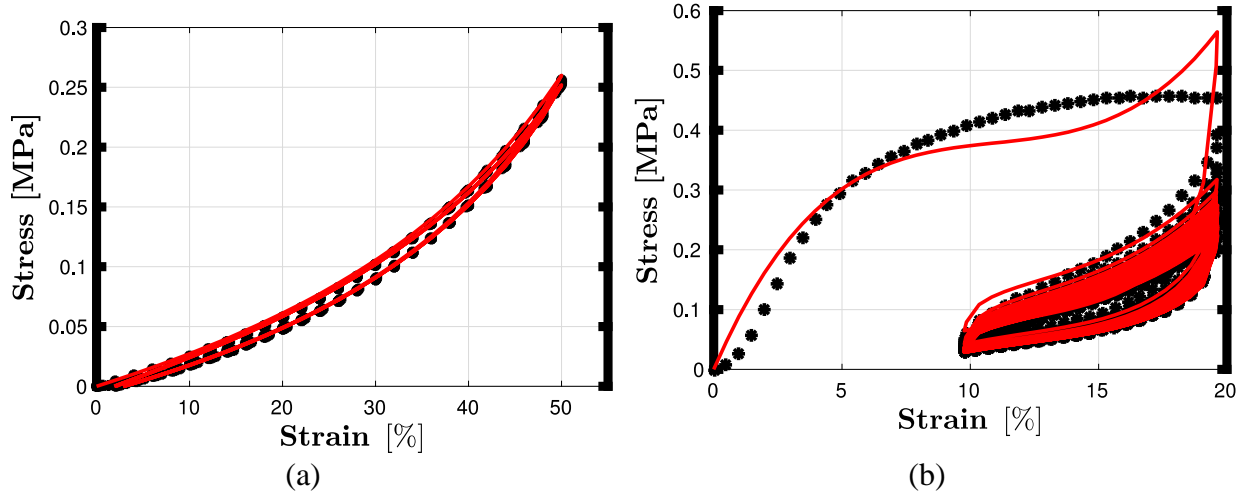


Figure 30. Calibration results for Pure Binder and P85 S085 A15 C00 specimens. The black dots indicate experimental data while red curve indicates calibrated model curve.

Table 5. Calibrated parameter values for the Pure Binder and P85 S085 A15 C00 specimens

	Pure Binder		P85 S085 A15 C00		
	1	2	1	2	3
μ_k	7.8435	0.1751	1.7442	0.1693	0.1522
α_k	1.0111	0.9037	9.5203	0.1296	1.4207
C_j	0.1488	0.0868	5.5029	0.6914	0.4216
γ_j	0.0012	37.2758	0.0021	0.0179	0.2244
c_m	722.988	1239.1341	370.6851	545.5946	219.2040
s_m	1.084	838.1424	61.2716	72.0798	215.0516
$\beta_{1,m}$	2741.9389	606.3938	5169.2	4.4	27.9
$\beta_{2,m}$	6740.8164	610.2029	601.1717	0.108	0.0227

Summary and Future Work

A finite-strain formulation for energetic composite materials, based on non-linear elasticity and yield surface-free endochronic plasticity, was presented, followed by an extensive experimental analysis of surrogate energetic material specimens. The analysis not only confirmed the existence of presumed properties, such as nonlinear behavior, permanent deformations and damage, cyclic hardening until stability, and loss of stiffness (instability) under monotonic loading, but was also successful in characterizing the material response based on sample composition, age and

specimen-to-specimen variability. Finally, a least squares-based minimization scheme was proposed to calibrate the model parameters using cyclic experimental data.

Our future tasks include

- Using the optimization algorithm to calibrate the parameters for various compositions using the complete cyclic data.
- Keep building the experimental database by performing compressive cyclic tests on the different surrogate material compositions at regular intervals.
- Characterizing the ageing behavior and sample-to-sample variability using the calibrated material parameters.

4.4 Crystal-Binder Interface Results

Figure 31 shows the temporal evolution of the maximum temperature on the surface of the polymer and the contour plots of temperature on the top surface of the specimen for cases (i) and (ii) (delineated in Section 3.5.1). Figure 32 shows the same results for cases (iii) and (iv). After 10 s there is a temperature increase of two degrees for case (i) and six degrees for case (ii) due to the change in the location of the heat source. The difference in temperature increases to 16 K when heat sources are placed on all of the particles, see Figure 32c. Therefore, uncertainty in the location of the heat source and on the source volume results in a large uncertainty on the temperature measured on the surface of the specimen (as is typically done in experiments). Due to the diffusive character of the heat equation, the fact that the temperature is measured on the top surface and that the particles are small compared with the sample size, the temperature contour plots on the surface have a circular shape. However, the value of the temperature and location changes with the location of the heat source, see Figures 31c and 32c. Therefore, the location and evolution of the heat sources in terms of the time dependent damage, geometry and loading conditions should be obtained.

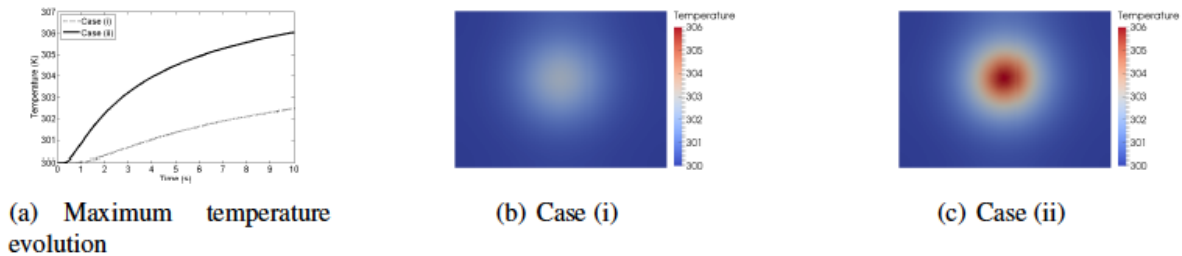


Figure 31. The simulated temperature on the top surface of the Sylgard block at $t = 10$ s for cases (i) and (ii)

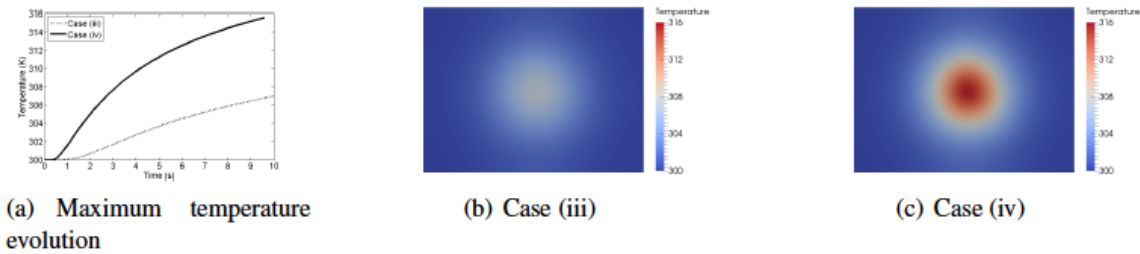


Figure 32. The simulated temperature on the top surface of the Sylgard block at $t = 10$ s for cases (iii) and (iv)

Note that the von Mises stress observed in the simulations remain below 30 MPa at any point in the domain. A value close to 30 MPa is only observed in the HMX particles close the interface between with the matrix. This value is much less than the yield strength of an HMX particle or the polymer considered. Thus, the plastic deformation and consequent heating can be neglected for the experiment modeled here. Although the dislocation pile-up mechanism has been proposed, they have been shown to be insufficient to generate meaningful heat. Dislocation pile-ups are configurations with several dislocations pinned at interfaces (grain boundaries) that suddenly move through plastic deformation avalanches. The work of Armstrong *et al.* [28] suggests that this is an important mechanism for hot spot formation. Others suggest that due to localization, pile-ups remain on a few adjacent atomic planes and therefore, this mechanism is insufficient to produce critical hot spot of sufficient size [27].

5. CONCLUSIONS

The research described herein has advanced the understanding of the near-resonant response of energetic materials to periodic loading through a joint analytical, numerical, and experimental investigation. The refined modeling tools developed with this improvement in basic understanding are currently being distilled and transferred to the Air Force Research Laboratory for Department of Defense use. Despite what are believed to be positive advancements, considerable work remains. In particular, additional research focus is warranted for systems excited at comparatively higher frequencies and those that utilize less traditional binder systems (e.g., those with a high degree of compliance or the converse) than those considered here. In addition, there is a need for continued development of the endochronic material model, further experimental validation of this model, and an exploration of how this model can be mathematically coupled with viscoelastic models. Finally, efforts should be made to distill lessons learned from crystal-scale computational models into structural-scale models via "effective material properties" or an alternate multi-scale approach.

6. REFERENCES

1. J. O. Mares, J. K. Miller, N. D. Sharp, D. S. Moore, D. E. Adams, L. J. Groven, J. F. Rhoads, and S. F. Son. Thermal and mechanical response of PBX 9501 under contact excitation. *Journal of Applied Physics*. 2013. **113**(8): 084904.
2. J. O. Mares, J. K. Miller, I. E. Gunduz, J. F. Rhoads, and S. F. Son. Heat generation in an elastic binder system with embedded discrete energetic particles due to high-frequency, periodic mechanical excitation. *Journal of Applied Physics*. 2014. **116**(20): 204902.
3. J. K. Miller, D. C. Woods, and J. F. Rhoads. Thermal and mechanical response of particulate composite plates under inertial excitation. *Journal of Applied Physics*. 2014. **116**(24): 244904.
4. D. C. Woods, J. K. Miller, and J. F. Rhoads. On the thermomechanical response of HTPB-based composite beams under near-resonant excitation. *Journal of Vibration and Acoustics*. 2015. **137**(5): 054502.
5. J. K. Miller, J. O. Mares, I. E. Gunduz, S. F. Son, and J. F. Rhoads. The impact of crystal morphology on the thermal responses of ultrasonically-excited energetic materials. *Journal of Applied Physics*. 2016. **119**(2): 024903.
6. J. Paripovic. Characterization and modeling of materials used in improvised explosive devices. M. S. Thesis. 2013. Purdue University.
7. N. P. Loginov, S. M. Muratov, and N. K. Nazarov. Initiation of explosion and kinetics of explosive decomposition under vibration [Translated]. *Combustion, Explosion, and Shock Waves*. 1976. **12**(3), p. 367-370.
8. N. P. Loginov. Structural and physicochemical changes in RDX under vibration. *Combustion, Explosion, and Shock Waves*. 1997. **33**(5), p. 598-604.
9. J. E. Field. Hot spot ignition mechanisms for explosives. *Accounts of Chemical Research*. 1992. **25**(11): p. 489-496.
10. B. L. Hamshere, I. J. Lockert, R. M. Dexter. Evaluation of PBXN-109: The explosive fill for the Penguin 12 anti-ship missile warhead. Systems Science Laboratory, Defense Science and Technology Organization. 2003. DSTO-TR-1471.
11. J. F. Rhoads, S. F. Son, P. Davies, M. Gonzalez, M. Koslowski, A. Range, J. Paripovic, A. Agarwal, B. Tanasoiu, J. Palsdottir. Near-resonant thermomechanics of energetic and mock energetic composite materials. 2016. DTIC Document AD1025771.
12. R. W. Ogden. Large deformation isotropic elasticity-on the correlation of theory and experiment for incompressible rubberlike solids. *Proceedings of the Royal Society of London. A. Mathematical and Physical Sciences*. 1972. **326**(1567): p. 565-584.
13. R. W. Ogden. Large deformation isotropic elasticity-on the correlation of theory and experiment for compressible rubberlike solids. *Proceedings of the Royal Society of London. A. Mathematical and Physical Sciences*. 1972. **328**(1575): p. 567-583.
14. K. C. Valanis. A theory of viscoplasticity without a yield surface, Part I: General theory. *Archives of Mechanics*. 1971. **23**: p. 517-551.
15. C. Suchocki. An internal-state-variable based viscoelastic-plastic model for polymers. *Journal of Theoretical and Applied Mechanics*. 2015. **53**(3): p. 593-604.
16. J. Paripovic and P. Davies. Identification of the dynamic behavior of surrogate explosive materials. *ASME 2013 International Design Engineering Technical Conferences and Computers and Information in Engineering Conference*. 2013. DETC2013-12755.

17. J. Paripovic and P. Davies. Characterizing the dynamics of systems incorporating surrogate energetic materials. *Special Topics in Structural Dynamics, Volume 6. Conference Proceedings of the Society for Experimental Mechanics Series*. 2016. p. 101-109.
18. J. Paripovic and P. Davies. A model identification technique to characterize the low frequency behavior of surrogate explosive materials. *Journal of Physics: Conference Series*. 2016. **744**(1): 012124.
19. H. C. Wu and M. C. Yip. Endochronic description of cyclic hardening behavior of metallic material. *Journal of Engineering and Materials Technology*. 1981. **103**(3): p. 212-217.
20. W. C. Yeh. Verification of the endochronic theory of plasticity under biaxial load. *Journal of the Chinese Institute of Engineers*. 1995. **18**(1): p. 25-34.
21. H. Y. Lin, W. C. Yeh, and W. J. Lee. A material function of endochronic theory and its application to test under axisymmetrically cyclic loading conditions. *Journal of Mechanics*. 2007. **23**(2): p. 135-147.
22. F. P. Bowden, M. F. R. Mulcahy, R. G. Vines, and A. Yoffe. The detonation of liquid explosives by gentle impact. The effect of minute gas spaces. *Proceedings of the Royal Society of London. A. Mathematical and Physical Sciences*. 1947. **188**(1014): p. 291-311.
23. M. M. Chaudhri and J. E. Field. The role of rapidly compressed gas pockets in the initiation of condensed explosives. *Proceedings of the Royal Society of London. A. Mathematical and Physical Sciences*. 1974. **340**(1620): p. 113-128.
24. Z. A. Roberts, J. O. Mares, J. K. Miller, I. E. Gunduz, S. F. Son, J. F. Rhoads. Phase changes in embedded HMX in response to periodic mechanical excitation. *Challenges in Mechanics of Time Dependent Materials, Volume 2. Conference Proceedings of the Society for Experimental Mechanics*. 2017. p. 79-86.
25. J. K. Dienes. Frictional hot spots and propellant sensitivity. *MRS Symposium Proceedings*. 1983. 24: p. 373-381.
26. S. Flueckiger, Y. Zheng, and T. Pourpoint. Transient plane source method for thermal property measurements of metal hydrides. *ASME 2008 Heat Transfer Summer Conference collocated with the Fluids Engineering, Energy Sustainability, and 3rd Energy Nanotechnology Conferences*. 2008. HT2008-56311.
27. J. E. Field, N. K. Bourne, S. J. P. Palmer, S. M. Walley, J. Sharma, and B. C. Beard. Hot-spot ignition mechanisms for explosives and propellants. *Philosophical Transactions of the Royal Society of London A: Mathematical, Physical and Engineering Sciences*. 1992. **339**(1654) p. 269-283.
28. R. W. Armstrong. Dislocation mechanics aspects of energetic material composites. *Reviews on Advanced Materials Science*. 2009. **19**, p. 13-40.

A1. PERSONNEL IN THIS PERFORMANCE PERIOD

Name	Title	Project Role
Jeffrey F. Rhoads	Professor	PI
Steven F. Son	Professor	Co-PI
Patricia Davies	Professor	Co-PI
Marcial Gonzalez	Assistant Professor	Co-PI
Marisol Koslowski	Associate Professor	Co-PI
Allison Range	Graduate Research Assistant	Sample preparation and thermomechanical characterization
Jelena Paripovic	Graduate Research Assistant	Dissipative modeling and system identification
Ankit Agarwal	Graduate Research Assistant	Endochronic plasticity modelling
Akshay Dandekar	Graduate Research Assistant	Interface modeling
Lauren Cooper	Undergraduate Research Assistant	Sample preparation and thermomechanical characterization

A2. Publications and Presentations

List of Publication

1. A. R. Range, N. R. McMIndes, J. B. Tucker, and J. F. Rhoads. The influence of formulation variation and thermal boundary conditions on the near-resonant thermomechanics of mock explosives. *Fracture, Fatigue, Failure and Damage Evolution, Volume 7. Proceedings of the 2017 Annual Conference on Experimental and Applied Mechanics*. 2018. Springer: New York, New York. p. 47-55
2. A. Range, N. McMIndes, J. Tucker, and J. Rhoads. The influence of formulation variation and thermal boundary conditions on the near-resonant thermomechanics of mock explosives. The 2017 SEM Annual Conference. 2017. Indianapolis, Indiana.

List of Presentations

1. A. Range, N. McMIndes, J. Tucker, and J. Rhoads. The influence of formulation variation and thermal boundary conditions on the near-resonant thermomechanics of mock explosives. The 2017 SEM Annual Conference. 2017. Indianapolis, Indiana.

DISTRIBUTION LIST
AFRL-RW-EG-TR-2018-011

*Defense Technical Info Center
8725 John J. Kingman Rd Ste 0944
Fort Belvoir VA 22060-6218

AFRL/RWME (1)
AFRL/RWORR (STINFO Office) (1)